nanomaterials

MDPI

Review

Computational Methods for Charge Density Waves in 2D Materials

Sugata Chowdhury [1,2], Albert F. Rigosi [3], Heather M. Hill [3,4], Patrick Vora [5,6], Angela R. Hight Walker [3] and Francesca Tavazza [2,3,*]

1 Department of Physics and Astronomy, Howard University, Washington, DC 20059, USA; sugata.chowdhury@howard.edu
2 Material Measurement Laboratory, National Institute of Standards and Technology (NIST), Gaithersburg, MD 20899, USA
3 Physical Measurement Laboratory, National Institute of Standards and Technology (NIST), Gaithersburg, MD 20899, USA; albert.rigosi@nist.gov (A.F.R.); hmhill89@gmail.com (H.M.H.); angela.hightwalker@nist.gov (A.R.H.W.)
4 Physics Today, American Institute of Physics, College Park, MD 20740, USA
5 Quantum Science and Engineering Center, George Mason University, Fairfax, VA 22030, USA; pvora@gmu.edu
6 Department of Physics and Astronomy, George Mason University, Fairfax, VA 22030, USA
* Correspondence: francesca.tavazza@nist.gov

Abstract: Two-dimensional (2D) materials that exhibit charge density waves (CDWs)—spontaneous reorganization of their electrons into a periodic modulation—have generated many research endeavors in the hopes of employing their exotic properties for various quantum-based technologies. Early investigations surrounding CDWs were mostly focused on bulk materials. However, applications for quantum devices require few-layer materials to fully utilize the emergent phenomena. The CDW field has greatly expanded over the decades, warranting a focus on the computational efforts surrounding them specifically in 2D materials. In this review, we cover ground in the following relevant theory-driven subtopics for TaS_2 and $TaSe_2$: summary of general computational techniques and methods, resulting atomic structures, the effect of electron–phonon interaction of the Raman scattering modes, the effects of confinement and dimensionality on the CDW, and we end with a future outlook. Through understanding how the computational methods have enabled incredible advancements in quantum materials, one may anticipate the ever-expanding directions available for continued pursuit as the field brings us through the 21st century.

Keywords: density functional theory; charge density waves; transition metal dichalcogenides

Citation: Chowdhury, S.; Rigosi, A.F.; Hill, H.M.; Vora, P.; Hight Walker, A.R.; Tavazza, F. Computational Methods for Charge Density Waves in 2D Materials. *Nanomaterials* **2022**, *12*, 504. https://doi.org/10.3390/nano12030504

Academic Editor: Sotirios Baskoutas

Received: 15 December 2021
Accepted: 26 January 2022
Published: 1 February 2022

1. Introduction

Two-dimensional (2D) materials compose a rapidly evolving field within condensed matter physics, as well as related disciplines. More specifically, 2D materials that exhibit charge density waves (CDWs) have generated great interest, given the relevance of their exotic properties to various quantum-based technologies [1–6]. These materials are characterized by significant in-plane bonding and relatively weak out-of-plane van der Waals interactions, the latter of which allows for the isolation of individual monolayers through mechanical exfoliation. These monolayers can then enable the fabrication of many thin-layered devices that are capable of confirming properties and behaviors determined by computational methods.

A CDW is a quantum phenomenon that takes place in correlated systems [7–11], and the states exhibiting this phenomenon are of profound theoretical interest, since such states may provide a switchable function for tuning the electrical properties of customized devices. In short, the CDW state may be described as a periodic distortion of the atomic position, along with a corresponding modulation of the electron density, both of which

occur below a critical transition temperature [8]. The periodicity with which a CDW may be exhibited has two major forms. In the first form, the value takes on an integer multiple of the undistorted lattice constant (also called a commensurate CDW, or C-CDW). The second form, namely the incommensurate CDW (or IC-CDW), has an unrelated periodicity and typically has a much higher transition temperature. Once a material undergoes a phase transition at low enough temperature, the change in lattice periodicity is accompanied by a localized band-splitting at the Fermi level, lowering the overall energy of the system.

Experimental and theoretical investigations into CDW phase transitions started over 50 years ago and focused mostly on a special class of materials known as transition metal dichalcogenides (TMDs). Among the efforts were those that explored the theory behind CDW formation and behavior [12–20]; motion and transport properties [21–25]; and several other experimental works [26–28], including neutron scattering [29], impurity pinning [30], and thermal properties [31]. Moreover, two major phases of TMDs were primarily focused on: 1*T* and 2*H*. A simple way to visualize the difference between these two phases is that the 1*T* phase has a planar cross-section that may be described as more rhombic than its 2*H* phase counterpart. Some prime examples of calculations performed on these materials are shown in Figure 1. During this first major wave of research efforts, work was performed by involving systems that exploited the nature of electrons in 2D environments [32–34]. Through the 1990s and early 2000s, the work focused dominantly on a few material families of TMDs, paving the way for a fuller theoretical understanding of the origins, characteristics, and applications of CDW states [35–46].

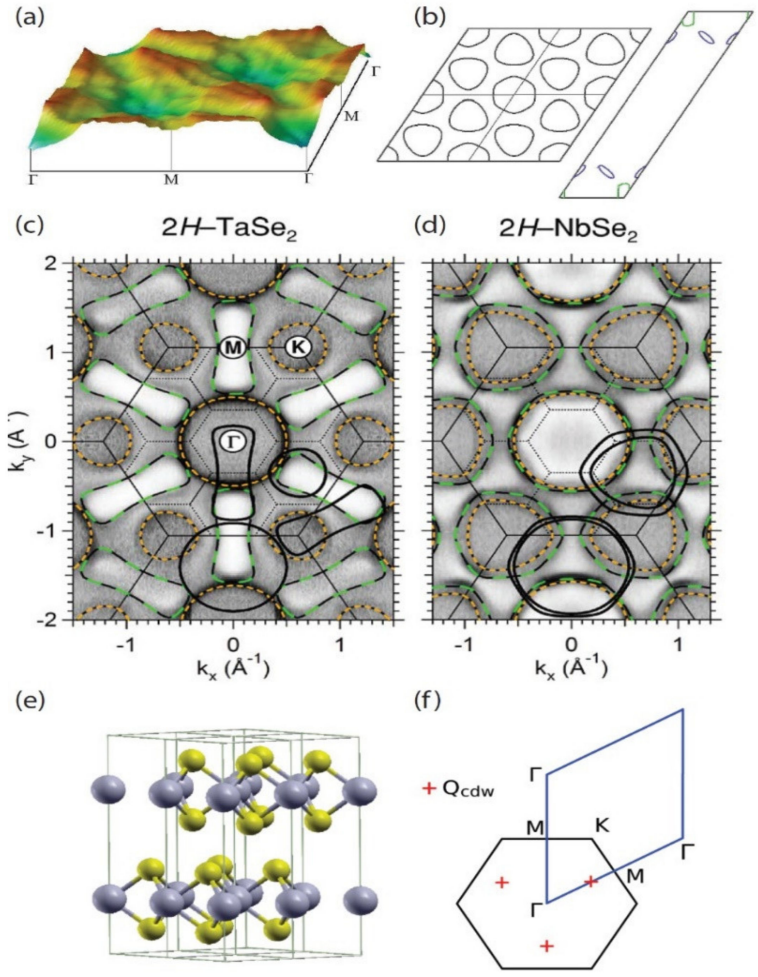

Figure 1. (**a**) Real part of the bare static electronic susceptibility (in arbitrary units) with constant matrix elements. This was calculated by using the band structure of monolayer $NbSe_2$. (**b**) The corr-

esponding Fermi surface is shown. (**c**) Angle-resolved photoemission spectroscopy (ARPES) intensity maps of 2*H*-$TaSe_2$ and (**d**) 2*H*-$NbSe_2$ are shown at 125 and 65 K. The darker grayscale indicates higher photoemission intensity. The small-dotted hexagons are the Brillouin zone scheme for the super-lattice. (**e**) The crystal structure and Brillouin zone are shown for 2*H*-$TaSe_2$. The large spheres (gray) correspond to Ta atoms, and the small spheres (yellow) represent Se atoms. (**a**,**b**) Reprinted figure with permissions from Reference [46]. Copyright 2009 by the American Physical Society. (**c**,**d**) Reprinted figure with permissions from Reference [41]. Copyright 2005 by the American Physical Society. (**e**,**f**) Reprinted figure with permissions from Reference [47]. Copyright 2012 by the American Physical Society.

Within the modern era of theoretical research on CDWs in TMDs, it became evident that, in order to utilize quantum devices constructed from few-layer material, a comprehensive examination of device behaviors with a variety of computational methods, such as density functional theory (DFT), was crucial. These quantitative assessments of the observations made in these material systems became vital for future efforts to realize quantum information platforms based on non-equilibrium phenomena [48,49]. It also became clear that a large variety of material systems was available for computing general physical phenomena. One nice example of the computational abilities developed was to calculate Fermi surfaces for these materials, such as those shown in Figure 2. Within the last decade, there have been many theoretical and experimental results reported on the following TMD material systems: $NbSe_2$ [50–54], NbS_2 [55–60], TiS_2 [61–65], $TiSe_2$ [66–71], VS_2 [72–76], and VSe_2 [77–81].

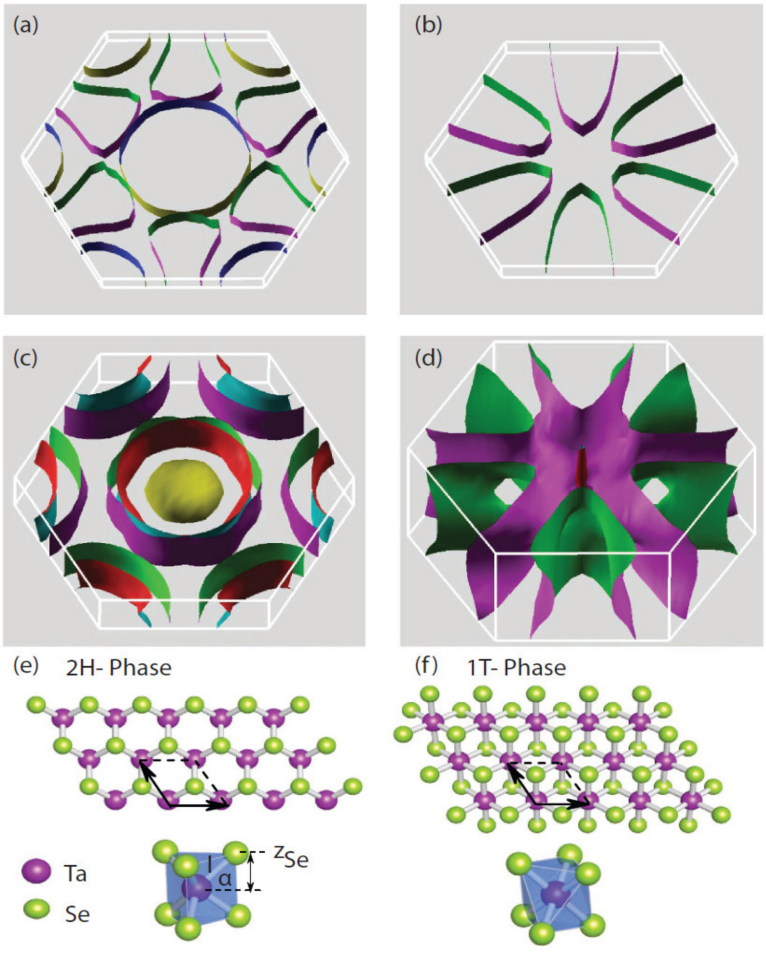

Figure 2. (**a**) Fermi surfaces are calculated for monolayer 2*H*-$TaSe_2$, (**b**) monolayer 1*T*-$TaSe_2$, and (**c**,**d**) their respective bulk counterparts with spin–orbit coupling (SOC) explicitly included [82]. The

crystal structures of monolayer $TaSe_2$ are shown for the (**e**) 2*H* phase and the (**f**) 1*T* phase. Reference [82] is an open-access article distributed under the terms of the Creative Commons CC BY license, which permits unrestricted use, distribution, and reproduction in any medium.

The sizeable number of pursuits surrounding these materials renders any attempt at compiling every use or research effort impractical, so, instead, this review covers the following relevant theory-driven subtopics for the materials systems $TaSe_2$ and TaS_2: summary of general computational techniques and methods, atomic structure, Raman modes, and effects of confinement. The review also focuses primarily on theoretical work, with appropriate context and some supporting experimental efforts that ultimately validate some of the efforts described herein. Through understanding how such computational methods have enabled incredible advancements in quantum materials, one may anticipate the ever-expanding directions available for continued pursuit as this field brings us through the 21st century.

2. Computational Techniques and Methods

DFT can accurately predict the electronic and phononic structures of various materials and allows for the use of larger computational cells, which, in turn, are key to successfully carrying out a model for CDW phase transitions [46,54,83–85]. However, there are a couple of obstacles to overcome when using DFT for such purposes. The first obstacle is intrinsically related to some of the properties used in DFT: for instance, all standard DFT calculations are performed at the thermal temperature of 0 K, whereas phenomena such as the CDW phase transitions are inherently temperature-driven. A second obstacle presents itself during the use of plane-wave DFT codes. Sometimes, CDW phases have periodic cells that are incommensurate (I-CDW), thereby making any modeling of a phase transition a rather non-trivial problem if periodic boundary conditions are imposed. A third obstacle that can arise before starting any simulations is the choice of appropriate DFT parameters. The most suitable psedo-potential/exchange-correlation functional must be selected, as well as the appropriate *k*-point density determined by a metric of high convergence. Such choices are, obviously, not unique to the CDW modeling, but are of high importance here, as the system response is very sensitive to these parameters. In the rest of this section, we briefly review how these points were dealt with in the case of 2*H*-$TaSe_2$ and 2*H*-TaS_2.

Some DFT results presented throughout the review were carried out by using the Quantum ESPRESSO (QE) package [86–88], and this is widely seen as a versatile tool for DFT work. There are many other approaches and details that can make a DFT approach more suitable over others depending on the material system. Other techniques can include the exchange-correlation interaction being described by local density approximations, using Perdew–Wang correlation [89], norm-conserving pseudopotentials [90,91], and van der Waals corrections [92–95]. More details on the DFT methodology can be found in additional related work [96–104].

Though there are a variety of approaches for including finite temperature in DFT simulations, such as DFT-MD or finite-temperature DFT, their computational cost is significantly larger than that of exact DFT, making them difficult to use for larger simulations, such as those required for investigating CDW transitions. An alternative approach to avoid this problem of temperature is to model the formation of the CDW states by only changing the system's electronic temperature rather than concerning oneself with the thermal temperature. In order to qualitatively assess the effect of temperature on the phonon properties of the system and the Kohn anomaly [46,54,105–107], a smearing factor, σ, which is a parameter characteristic of the Fermi–Dirac distribution associated with a certain temperature, must be introduced. This approach of modeling real temperature effects with electronic temperature variations is computationally inexpensive and can be validated by using secondary means, such as comparing the lattice expansion as a function of temperature for theoretical and experimental cases.

As an example, the case of $TaSe_2$ is shown in Figure 3 [108]. Here, DFT findings reproduce qualitative changes for both the *a* and *c* lattice constants compared to the experiment

and are also close to being quantitatively correct. The maximum relative change for a is 1.5% experimentally and 1.1% in the DFT evaluation. The thermal evolution of lattice constant, c, is not as accurate but still completely acceptable (4.1% experimentally and 2.3% computationally). Even in the more complex case of TaS_2 (Figure 4), the thermal evolution trend is well-reproduced with this approach of only using the electronic temperature [109].

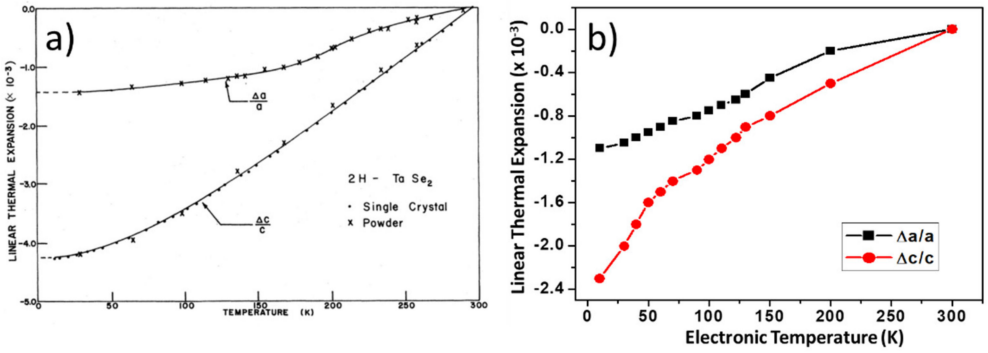

Figure 3. Comparison between (**a**) experimental [97] and (**b**) DFT [108] lattice expansion for $TaSe_2$ when the temperature dependence is introduced in the DFT modeling solely through changes in the electronic temperature. Reprinted figure with permissions from Reference [97]. Copyright 1978 by the American Physical Society. Reprinted figure with permission from Reference [108]. Copyright 2019 by the American Physical Society.

Though some materials, such as 2H-$TaSe_2$, have a CDW phase commensurate to their room temperature lattice, that is not always the case. On the other hand, 2H-TaS_2 is an example of a compound with an IC-CDW phase. Modeling the transition between the room temperature and incommensurate structure is not straightforward if periodic boundary conditions are used. To circumvent such a problem, Janner et al., suggested that it is possible to apply a perturbation along the c axis in the form of small compressive stress to computationally model incommensurability, using a relatively small cell [99]. This strategy was successfully applied in Reference [108], using a $3 \times 3 \times 1$ cell and a -0.3% strain to keep the c lattice constant when changing with temperature. From this work, stressed and unstressed Raman modes were predicted (see Table 1). Comparisons among the two DFT treatments and the experimental data for all temperatures and for such a mode are shown in Figure 5.

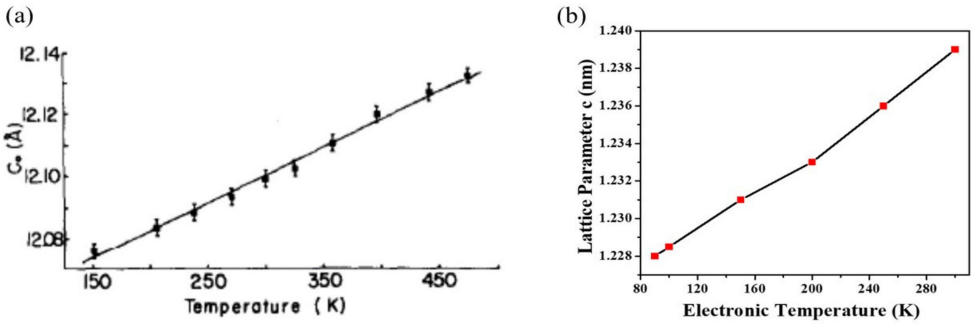

Figure 4. Thermal expansion of the c lattice constant for TaS_2. (**a**) The experimental data are found in Reference [98]. (**b**) Relevant computational result may be found in Reference [109]. The linear trend seen in the experimental findings is well reproduced in the DFT modeling by using only the electronic temperature. Reprinted figure with permission from Reference [109]. Copyright 2019 by the American Physical Society.

Table 1. A comparison of experimental and simulated Raman modes from References [99,109] for both the stressed and unstressed cases. The X indicates a missing value in the literature.

Mode (cm^{-1})	Exp—4 K	10 K	30 K	50 K	60 K	300 K
E^2_{2g}(shear)—Stressed	26	30.7	X	X	X	32.8
$^2E_{2g}$ (CDW)—Stressed	51	48.8	46.6	44.6	42.8	X
$^1A_{1g}$ (CDW)—Stressed	79	76.0	67.6	63.0	62.6	X
E^2_{2g}(shear)—Unstressed	26	34.9	32.3	33.6	32.0	31.8
$^2E_{2g}$ (CDW)—Unstressed	51	42.4	42.2	39.1	38.1	36.1
$^1A_{1g}$ (CDW)—Unstressed	79	80.4	80.0	76.3	75.3	75.1

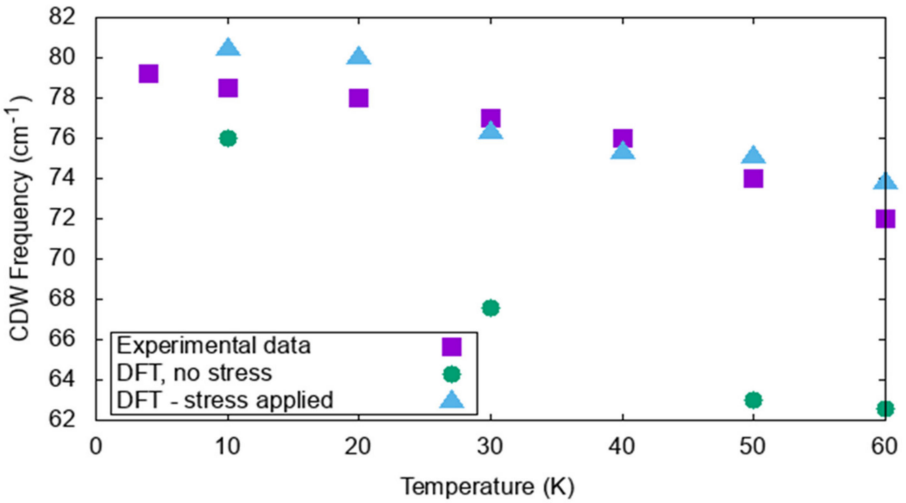

Figure 5. Temperature dependence of the experimentally observed CDW mode at 79 cm^{-1}. Including incommensurability through a small compression in the simulation cell (triangular data) leads to an excellent reproduction of the experimental data.

The last key point that needs careful consideration when performing computational modeling of Raman spectra for CDW materials is the choice of exchange-correlation functional, as well as pseudopotential. While this is not the place for a complete investigation of such variables, as an example of its importance, the variability of results that such a choice brings is exemplified in the case of $TaSe_2$. Table 2 displays some of these findings for lattice constants and Raman modes (for the unit cell) under various computational choices.

Table 2. Raman modes for $TaSe_2$ unit cell. As the average error (computed as the average of the absolute differences between experimental and DFT result for each mode) shows at a glance, using LDA with PW parametrization leads to Raman frequencies overall closer to the experimental ones.

Raman Modes	E_{1g}	E^1_{2g}	E^2_{2g}	A_{1g}	Average Error
Exp. (Reference [110])	136	210	210	239	—
GGA (PBE-Norm)	147.0	206.3	206.3	237	5.1
LDA (PZ-Norm)	142.5	203.9	203.9	233	6.2
GGA (PW)	142	197	197	226	11.2
LDA (PW)	141.3	212.4	212.4	241.8	3.2
GGA (PBE-Ultra)	129.8	199.5	199.5	229.4	9.2
LDA (PZ-Ultra)	133.6	207.7	207.7	227.4	4.7
GGA (PBE-PAW)	125.1	198.9	198.9	230.2	10.5

As one can see from Table 2, there are two main computational approaches being exemplified. The first approach is the use of the local density approximation (LDA). Within the LDA, Perdew–Wang (PW) and Perdew–Zunger (PZ) exchange and correlation functionals were used and; in some cases, the van der Waals density functional (vdWDF) is used to capture non-local correlations. Some works used a scalar relativistic norm-conserving pseudopotential [90,91]. The second main computational approach is the use of the general-gradient approximation (GGA), which tends to reproduce lattice constants better than the LDA. Within the GGA, sub-methods include the use of projected augmented wave (PAW) code or the Perdew–Burke–Ernzerhof (PBE) method. Ultimately, Raman frequencies are better modeled by using the LDA, with the smallest average error (average of the absolute difference between experimental data and DFT) being found for the PW correlation and norm-conserving pseudopotential [90,91].

3. Computational Results in Atomic and Band Structures

The computational techniques and methods described in the previous section have all been applied in the variety of works surrounding TMDs. For the next sections, results obtained from the use of these methods are summarized and organized by material system.

3.1. TaS_2 Structure

There has been plenty of work on TaS_2 bulk systems, much of which uses some computational methods that have evolved into the familiar methods summarized earlier [111–113]. Regarding 2D TaS_2, several groups use computational methods to answer questions involving this CDW material and its structures. For instance, Lazar et al., analyzed the structure of thin TaS_2, focusing on the 1*T* and 2*H* phases [114,115]. A commensurate charge density wave phase was derived from first principles, and both the vdW interaction and electron–electron interactions were included by using the exact exchange approximation (EXX) as well as the random phase approximation (RPA). These DFT calculations were performed by using the PAW method implemented in VASP. Lazar et al., calculated the total energy by summing the exact exchange energy and RPA correlation energy, as demonstrated in Figure 6.

Hinsche et al., investigated the influence of electron–phonon coupling on the electronic transport properties of both bulk and monolayer TaS_2. Much of the work was based on density functional perturbation theory (DFPT) and semi-classical Boltzmann transport calculations. The work reported promising room-temperature mobilities and sheet conductances [116]. Though they focus on just the H-polytypes, their work implements sophisticated mathematics needed for vdW forces, namely the optB86b-vdW functional. There have been other efforts to include vdW interactions into various sample geometries [117].

Sanders et al., performed DFT calculations for freestanding single-layer TaS_2 via VASP code [118]. Others, such as Kresse et al. [104], have also heavily relied on VASP code for similar calculations. For this picture, valence electrons were described by plane-wave basis sets with a kinetic energy threshold of 415 eV, and the exchange-correlation functional was approximated with the PBE method. To give validity to their calculations, single-layer TaS_2 was epitaxially grown on Au(111) substrates, and this yielded 2D 1*H* polymorphs. These samples were subsequently measured by angle-resolved photoemission spectroscopy (ARPES) and found to be in agreement with DFT calculations, as shown in Figure 7 [118].

Lastly, as DFT methods improve for lower-dimensional systems, the pursuit of understanding the physics in quasi-2D systems becomes warranted. Cain et al., performed DFT calculations on 2*H*-TaS_2 nanoribbons to determine if any periodic features arise from CDW-type distortions [119]. Other linear chain systems had been explored in earlier theoretical work [18,21,25], but nanoribbons were not included in this initial effort. It turned out that the DFT calculations indicated that CDW states were supported by the nanoribbon geometries, albeit with amplitudes that were small. They also observed dramatic zigzag

superstructures, though only as a result of the linear defect arrays, whose atomic structure was calculated via first principles. These results can be seen in Figure 8.

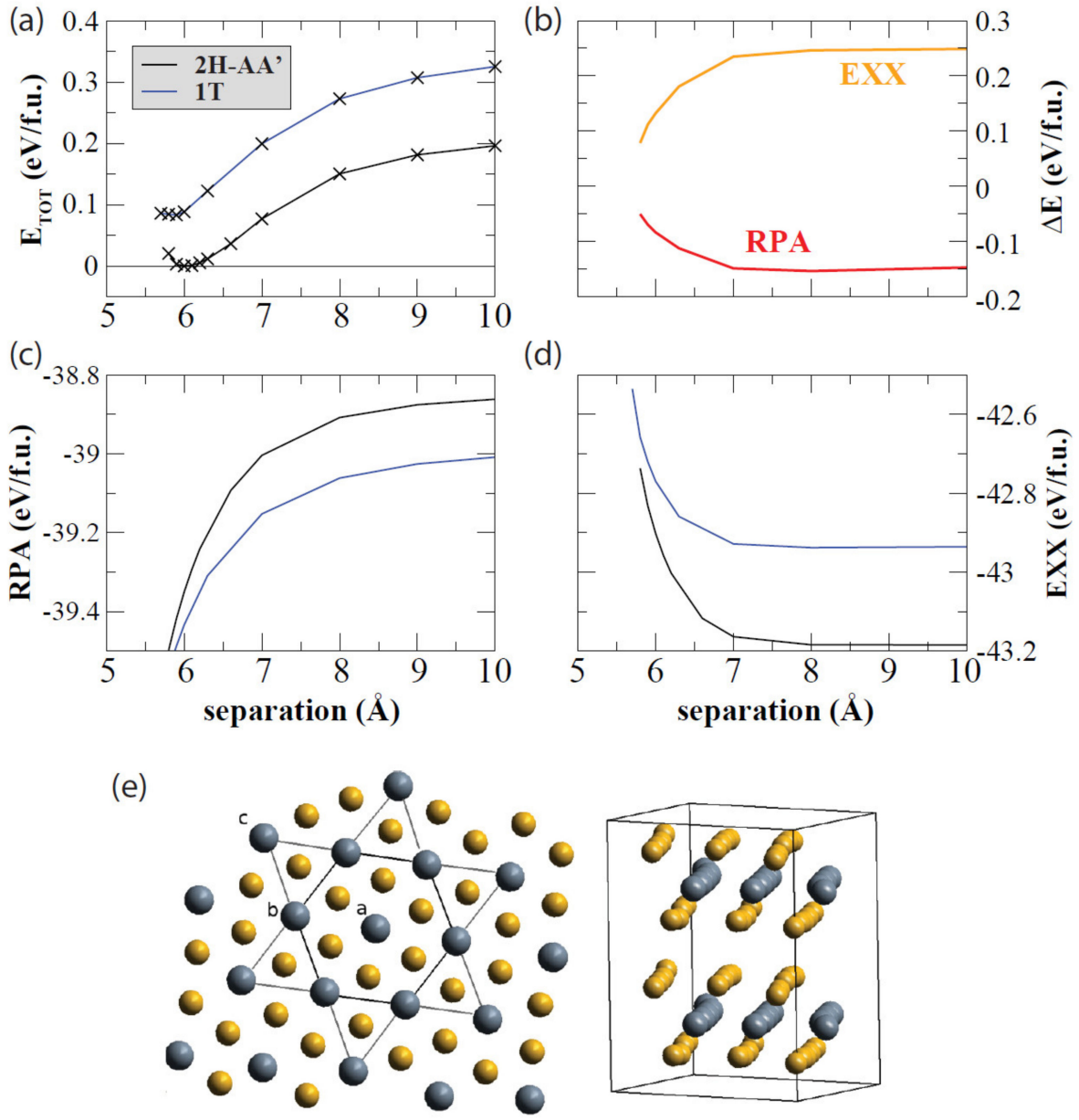

Figure 6. Decomposition of the total energy as a function of the separation of the S-Ta-S layers for the 1*T* and 2*H* polytypes is shown and plotted as such: (**a**) the total energy, (**b**) the RPA correlation energy, (**c**) the difference in the polytypes' exact-exchange (EXX), and RPA energies (**d**) EXX. (**e**) The starlike arrangement of the atoms in the C-CDW phase from the in-plane view (**left**) and from the side view (**right**). Reprinted figure with permission from Reference [114]. Copyright 2015 by the American Physical Society.

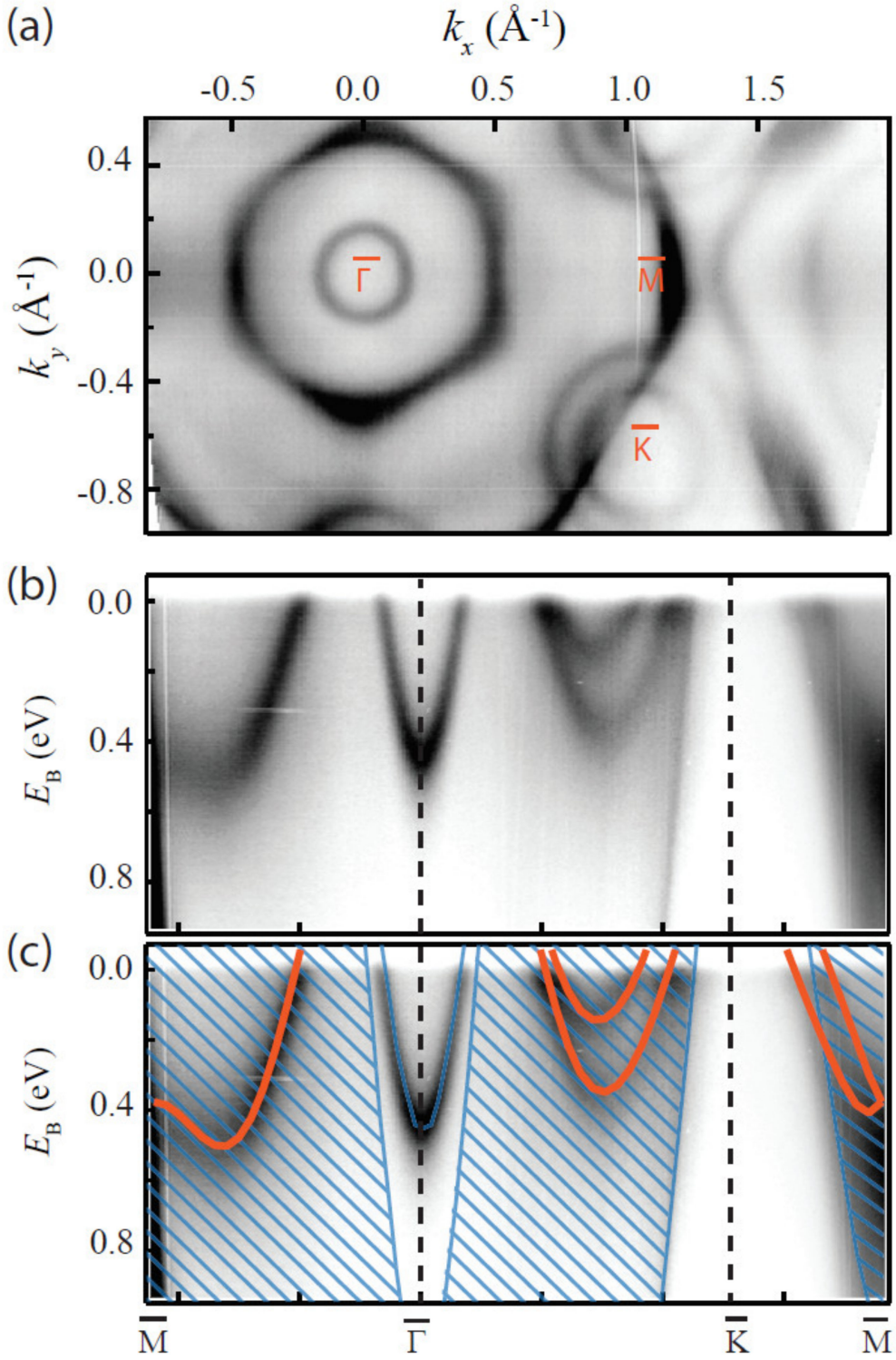

Figure 7. Electronic structure of monolayer TaS_2 measured with ARPES. (**a**) Photoemission intensity at the Fermi energy. (**b**) Photoemission intensity along high-symmetry directions of the 2D Brillouin zone. (**c**) Data in (**b**) with the calculated 1*H*-TaS_2 band structure superimposed in orange. The calculated bands were shifted by 0.12 eV to higher binding energy. The Au surface state and projected bulk bands of Au(111) are indicated with blue, as guides to the eye. Reprinted figure with permission from Reference [118]. Copyright 2016 by the American Physical Society.

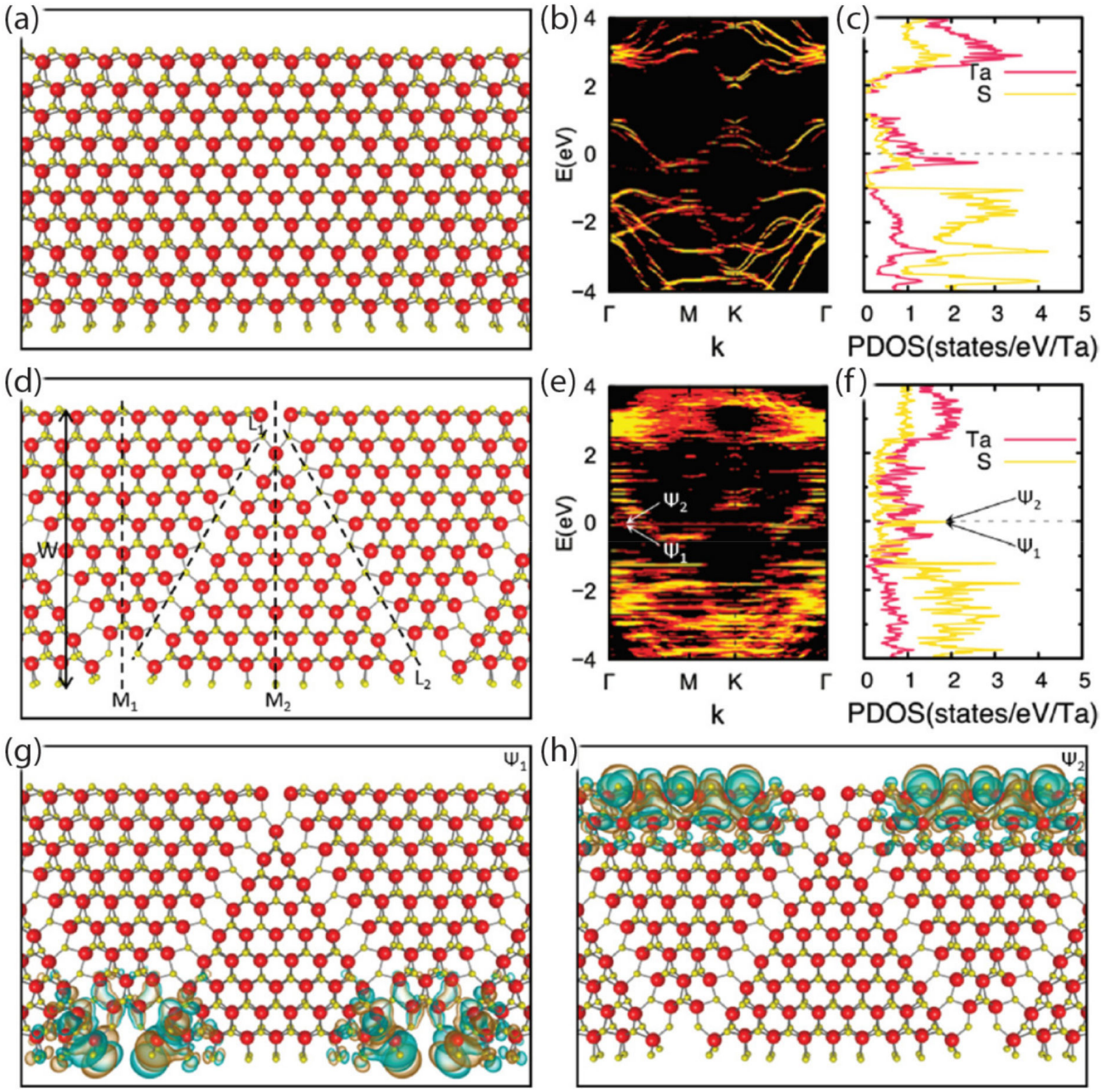

Figure 8. Atomic and electronic structure of TaS_2 nanoribbons as shown by Cain et al. [119]. (**a**) The planar atomic structure of a 2.99 nm–wide nanoribbon is shown without the zigzag defect, whose CDW distortions are too small to be seen. (**b**) The electronic band structure is shown. (**c**) The partial density of states (PDOS, DOS) of the nanoribbon is plotted. (**d**) A planar view of the atomic structure of a 3.08 nm–wide nanoribbon is shown, with zigzag boundaries of S vacancies represented by black dashed lines denoted as L1 and L2. (**e**) The electronic band structure and (**f**) the PDOS of the nanoribbon are calculated. Localized edge states are denoted as ψ_1 and ψ_2. Structures in (**g**,**h**) show real-space wave functions of those localized edges states, with isosurfaces for the positive and negative wave function values shaded in cyan and orange, respectively. Ta and S atoms are represented by red and yellow spheres, respectively. Reprinted with permission from Reference [119]. Copyright 2021 by the American Chemical Society.

3.2. $TaSe_2$ Structure

Similar to the case of TaS_2, work on bulk systems was plentiful in the decades preceding the experimental realization of 2D crystal exfoliation [120–126]. Once it became possible to probe lower dimensional systems, many efforts sought to fully understand CDW states in $TaSe_2$. Samankay et al., reported DFT calculations involving a reduced Brillouin zone of the C-CDW structure resulting from lattice reconstruction in monolayer $TaSe_2$. For their calculations, this reduced zone formed a subset of the normal Brillouin zone of undistorted $TaSe_2$. Specifically, some dozen points in the normal set were mapped to the Γ point of the reduced set. Figure 9 shows these dozen points and the general phenomenon of zone-folding. Any modes derived from this zone-folding phenomenon can result in measurable Raman spectral peaks [127].

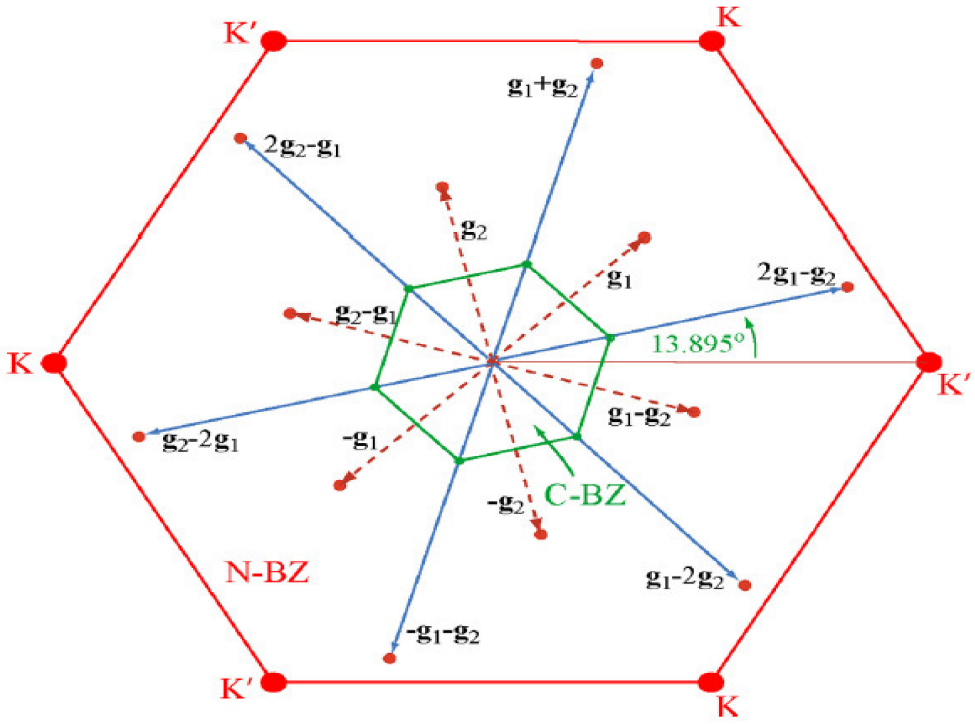

Figure 9. Normal (red) and commensurate reconstructed (green) Brillouin zone of monolayer 2*H*-$TaSe_2$. The equivalent Γ points in the first extended Brillouin zone and second extended Brillouin zone are connected to Γ by red and blue vectors, respectively. Reprinted with permission from Reference [127]. Copyright 2015 by the American Chemical Society.

In other work, such as that by Ge and Liu [47], the structural, electronic, and vibrational properties of both bulk and single-layer 2*H*-$TaSe_2$ were investigated by using first principles. They found that CDW instability remains present even after removing interlayer interactions from the performed calculations. It was also found that the Fermi surfaces of single-layer materials exhibit a strong sensitivity to spin–orbit coupling (SOC). For most of their results, the electron–core interaction was described by scalar relativistic ultrasoft pseudopotentials [47]. These calculations were performed with a plane-wave energy cutoff of 35 Ry, a 18 × 18 × 6 uniform mesh of *k* points, and the Vanderbilt–Marzari Fermi smearing method for accelerated convergence. The same group went on to perform a set of calculations based on pressure dependence, with later work including the effects of electron doping [128,129].

The general understanding of calculations for these CDW materials gains a solid backing when they are complimented by extensive experimental work, as seen in the case of Ryu et al. (includes Figure 10 below) [130]. This work shows the characterization results of single-layer 1*H*-$TaSe_2$, using ARPES, STM/STS, and DFT. A 3 × 3 CDW order was shown

to persist despite numerous distinct changes in the low-energy electronic structure and corresponding modifications to the topology of the Fermi surfaces. Enhanced SOC and lattice distortion were found to be a crucial component in the formation of this observed CDW order. Additional calculations include the interface structure between $TaSe_2$ and graphene, which was a used substrate. Calculating structures on other substrates, especially layered ones, such as epitaxially grown graphene, which has an interfacial buffer layer [131], has become increasingly accessible due to efforts such as these. Ryu et al., continued by describing the intricacies of how Fermi surfaces change from these interactions.

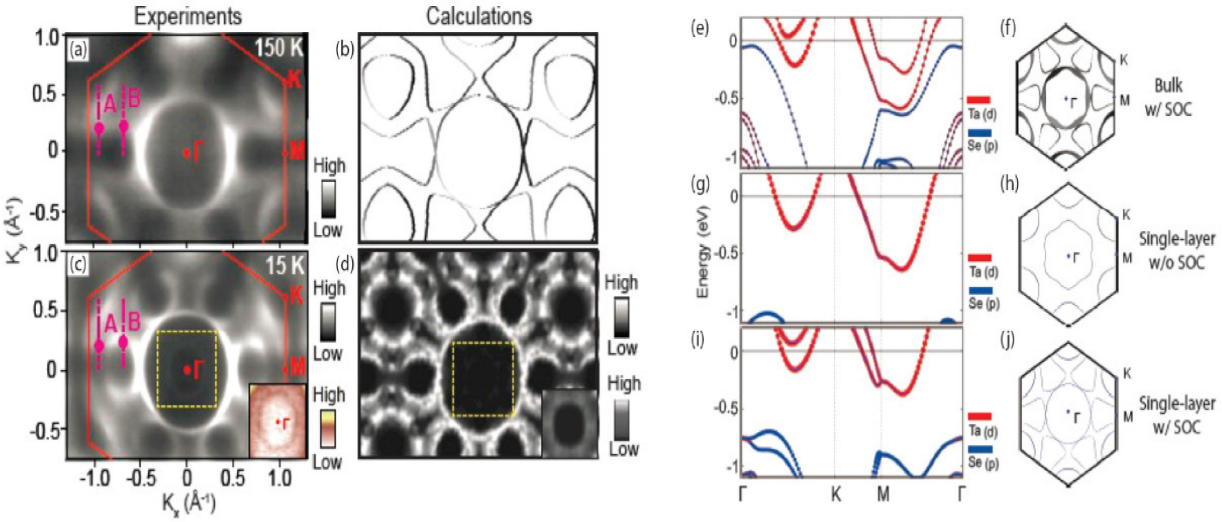

Figure 10. Electron-band structure and Fermi surface of $TaSe_2$. (**a**) ARPES and (**b**) calculated Fermi surface map in the normal state (150 K). (**c**) ARPES and (**d**) calculated Fermi surface for the CDW state (15 K). Solid lines in panels (**a**,**c**) mark the 2D Brillouin zone of $TaSe_2$. Insets at the right bottom corner in (**c**,**d**) are the region marked by yellow dotted square around Γ with different color scales. Calculated band structure and Fermi surface of normal-state $TaSe_2$ in its (**e**,**f**) bulk form with SOC, (**g**,**h**) monolayer form without SOC, and (**i**,**j**) monolayer form with SOC. Reprinted with permission from Reference [130]. Copyright 2018 by the American Chemical Society.

Based on the work by Yan et al. [82], DFT calculations can yield DOS information for monolayer $TaSe_2$. The crystal structures of 2*H* and 1*T* phases predictably lead to electronic band dispersions that exhibit visually distinct features, as shown in Figure 11a,c. These plots are a good example of how DFT can help with distinguishing the different phases of various 2D materials. In the case of $TaSe_2$, the distinctions in band dispersion near the Fermi level originate from the Ta atom 5*d* orbitals under the influence of the six nearest-neighbor Se atoms; this is a characteristic that is not present in the 1*T* case. Our last example of the usefulness of DFT calculations in understanding the atomic and electronic structures of monolayer $TaSe_2$ comes from Park et al. [132]. In their work, a discrepancy and expanded structural degree of freedom is understood in the case where a CDW unit cell contains thirteen Ta atoms. They go on to describe the coexistence of different CDW structures in the literature and, further, suggest the anion-centered structural model as the prime atomic structure candidate of the CDW state of monolayer 1*T*-$TaSe_2$. This model reproduces all observed spectroscopic features and addresses the case of SiC-caused electron doping. Overall, the heavy focus on $TaSe_2$ grants it legitimacy as a material that may provide significant progress in the development of quantum-based technologies.

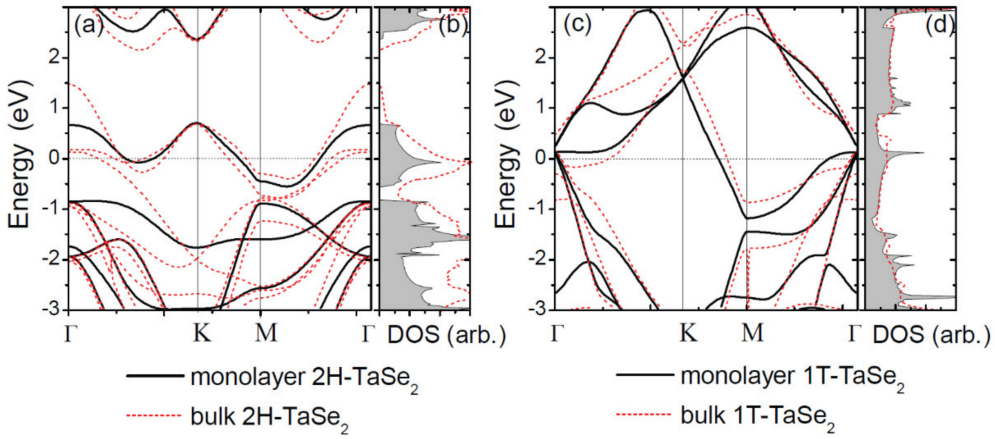

Figure 11. (**a**) Electronic-band structure and (**b**) the DOS for monolayer 2*H*-$TaSe_2$. (**c**,**d**) Results for monolayer 1*T*-$TaSe_2$. Band structures and the DOS of bulk are shown as red dashed lines. The Fermi level was shifted to zero. Reference [82] is an open-access article distributed under the terms of the Creative Commons CC BY (https://creativecommons.org/licenses/ (accessed on 14 December 2021).) license, which permits unrestricted use, distribution, and reproduction in any medium.

4. Theory-Driven Results in Raman Modes

It will benefit the reader to have a summary of how one goes about predicting Raman modes with DFT and other computational methods. One well-known method is to use the Plane-Wave Self-Consistent Field (PWscf) code within QE to calculate the phonon modes. The phonon-dispersion calculations based on the PWscf code were developed by using DFPT. Performing these calculations with this code generally involves three steps: (1) structural relaxation, (2) the SCF calculation, and (3) the final phonon dispersion using DFPT. Using post-processing tools, one may calculate a variety of properties from the phonon dispersion results, including, but not limited to, the interatomic force constants (IFCs), electron–phonon coupling coefficient for metals, dielectric constant and effective charge for non-metal crystals, phonon-dispersion band structure, and the phonon DOS.

For instance, in References [108,109], the ground-state structures of each crystal were determined by relaxing the bulk crystals' atomic positions and lattice vectors. The unit cell and supercell used a $16 \times 16 \times 16$ and $3 \times 3 \times 8$ k-point grid, respectively. Second, the SCF and phonon dispersion calculations were performed for each relaxed structure. Ultimately, these calculations computed the dynamical matrix on each point in q-space and used a $4 \times 4 \times 4$ uniform q-grid for the unit cell and only performed Γ-point phonon calculations for the supercell. Depending on the crystal symmetry, these latter calculations provided the vibrational frequencies or the eigenvalues of the dynamical matrix. Though one can obtain the modes' positions, the intensities were not provided by these calculations.

The dynamical matrix can also be used to compute the various aforementioned properties of the material. In these two references, the IFCs were calculated in real space, as well as the phonon-dispersion band structures and DOS. The dynamical matrix was also diagonalized by using the Acoustic Sum Rule in order to calculate the infrared and Raman cross-sections, and these steps were performed in the Molden and XCrySDen format. Using XCrysden visualization code, the vibration of the atoms was analyzed, ultimately revealing the nature and evolution of each Raman mode related to the CDW phase transitions.

Raman spectroscopy has been useful as an experimental technique for distinguishing the types of modes that can arise from the unique band structures of 2D materials. Furthermore, computational methods that yield realistic models of the physics behind these materials are more than capable of generating predictions of phonon behavior, with some being verifiable with experimental data. This section focuses primarily on how computational work has enabled the verification of phonon behaviors exhibited by TaS_2 and $TaSe_2$.

4.1. Phonon Behavior in TaS_2

Albertini et al., approached the computational analysis of phonon behavior in TaS_2 by employing support from experimental Raman data [133]. Their first-principles calculations of the vibrational properties of 1*T*-TaS_2 were performed for several thicknesses in both the undistorted and C-CDW phases (high and low temperatures, respectively). Raman spectra for bulk, few-layer, and monolayer samples at low temperatures were collected and used to support the notion that low-frequency folded-back acoustic modes can act as a convenient signature of the C-CDW structure in such spectra. The observations of low-frequency modes indicate that the commensurate phase continues to be the ground state even as the material is thinned to monolayer thicknesses.

In other work, such as Joshi et al.'s [109], the CDW transition is investigated with Raman spectroscopy, ARPES, and DFT, with a subset of the highlights shown in Figure 12. The study found that, below the CDW transition temperature, two CDW amplitude modes redshift and broaden with increasing temperature, and one zone-folded mode disappears. A two-phonon mode is also observed to soften with cooling, suggesting the presence of substantial lattice distortions at temperatures as high as 250 K. These observations, backed up by DFT predictions, are further confirmed with ARPES measurements showing the persistence of a CDW energy gap above the transition temperature. The finite-temperature DFT calculations of the phonon band structure indicated an instability occurring above the CDW transition temperature, along with providing atomic displacements of the CDW amplitude modes, reproducing their temperature-dependent behavior. The authors suggest that short-range CDW order exists above the transition temperature, generating new questions regarding the interplay between vibrational modes and electronic structures in layered CDW materials.

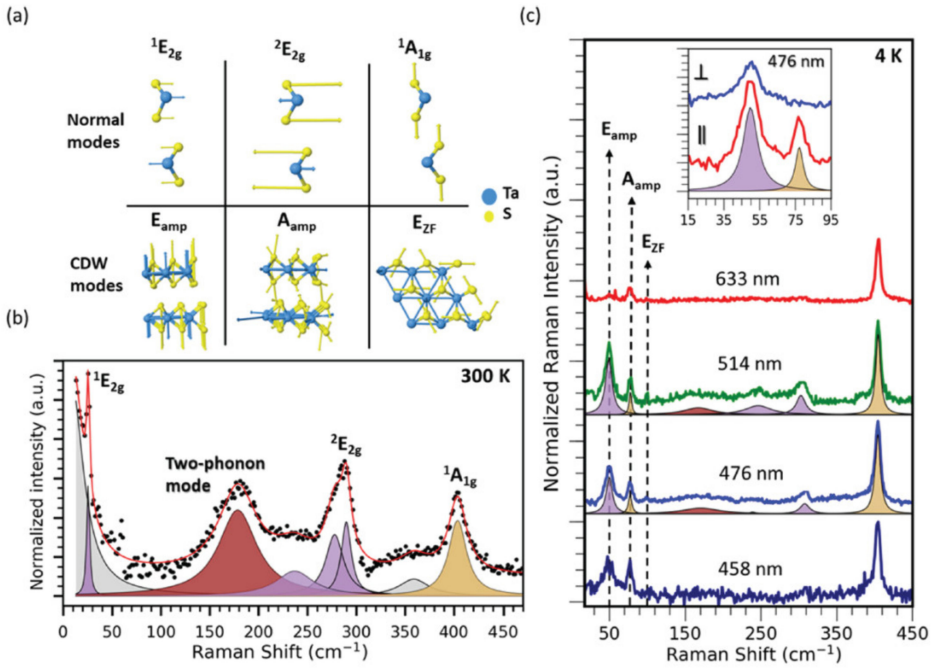

Figure 12. (**a**) Mode diagrams are shown and correspond to those seen in the normal and CDW phases. (**b**) Room-temperature Raman spectra of bulk TaS_2 reveals several modes. The two-phonon mode is shaded brown. Purple and golden shades represent modes with *E* and *A* symmetry, respectively. Gray areas represent fits to the laser Rayleigh line and other features not predicted to be part of the material's Raman spectrum. (**c**) Excitation-dependent Raman measurements performed at 4 K with 458, 476, 514, and 633 nm laser wavelengths. Low-frequency peaks correspond to CDW amplitude modes and a zone-folded CDW mode. Reprinted figure with permission from Reference [109]. Copyright 2019 by the American Physical Society.

Other work revolving around phonon dispersions has been reported by Hall et al. [134], where the calculations of phonon dispersions were based on a combination of DFT, DFPT, and many-body perturbation theory. The phonon self-energy was calculated, and this quantity encoded the renormalization of the dispersion due to interactions of the phonons with TaS_2 conduction electrons. They analyze how the interplay of electronic substrate hybridization, doping, and interlayer potentials affects the lattice dynamics and stability. This interplay is shown in Figure 13a, and, for example, the undoped (x = 0) and weakly hybridized (Γ = 10 meV) case hosts a longitudinal-acoustic (LA) phonon branch that exhibits a strong Kohn anomaly.

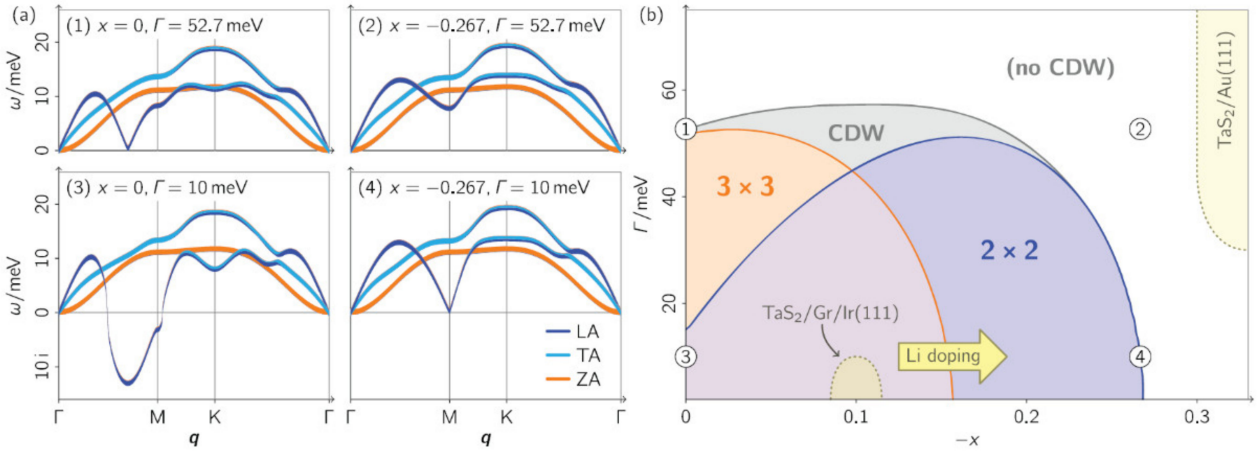

Figure 13. (**a**) Phonon dispersions and lattice instabilities of monolayer TaS_2 under different electronic conditions at 0 K (calculated). Acoustic phonon dispersions for different levels of hybridization with the substrate Γ (half width at half maximum of the electronic broadening) and charge doping x (electrons per Ta atom); $x < 0$ refers to electron addition. The character of the phonon modes, i.e., longitudinal (LA), transverse (TA), or out-of-plane (ZA), is marked in color. Imaginary phonon mode energies indicate that the lattice is unstable toward corresponding periodic lattice distortions. (**b**) Phase diagram of lattice instabilities in monolayer TaS_2. The CDW region is defined by the presence of an imaginary phonon energy. Regions with instabilities are shaded in color. Some experimentally realized situations are in the phase diagram. Reprinted with permission from Reference [134]. Copyright 2018 by the American Chemical Society.

The calculations by Hall et al., show that hybridization is a very effective destabilizer of charge order. To verify these calculations, monolayer TaS_2 was grown on Au(111) and verified with ARPES and STM. The calculations show that the hybridization is energy-dependent and that the half-width-at-half-maximum broadening spans a range between 30 and 90 meV. The monolayer TaS_2/Au(111) system was placed in the phase diagram of Figure 13b and accounts for the electron doping and the hybridization. Such interplay between these two phenomena stabilized the lattice, which can be further strengthened by lattice relaxation [135].

Interesting studies on the Star-of-David formations in the C-CDW state of TaS_2 are explored by Mijin et al. [136]. They used polarization-resolved high-resolution Raman spectroscopy to investigate the consecutive CDW regimes in 1*T*-TaS_2 single crystals, with the support of ab initio calculations. Their analysis of the C-CDW spectra reveals the symmetry of the system in such a way that the preferred stacking of the Star-of-David structure is trigonal or hexagonal. The spectra of the IC-CDW phase directly probed the phonon DOS, due to broken translational invariance. The temperature dependence of the symmetry-resolved Raman spectra indicated that the DOS exhibited a stepwise reduction in the CDW phases, followed by a Mott transition once within the C-CDW phase, with a corresponding Mott gap to be about 170 to 190 meV.

4.2. Phonon Behavior in $TaSe_2$

When it comes to efforts pertaining to $TaSe_2$, several groups have conducted extensive phonon studies with computational assistance. For instance, in the case of Hill et al., DFT calculations are utilized as implemented in the QE package [108]. The exchange-correlation interaction was described by LDAs, using the Perdew–Wang parametrization of the correlation energy [89]. Since the LDA exchange-correlation functionals yielded more reliable results when compared to experimental Raman data, as compared with the GGA [137], they became the standard for such sorts of calculations. Norm-conserving pseudopotentials were also utilized for describing the interactions between core and valence electrons.

Among their investigations was an analysis of the temperature dependence of the two-phonon mode and its origin. The required momentum for the two-phonon process came from transitions between a quasi-acoustic (QA) mode and a transverse optical (TO) mode [138–141]. The phonon band structure was computed by using a unit cell at seven electronic temperatures rather than the usual $3 \times 3 \times 1$ supercell [142–146], and the results allowed for the identification of the location of the Kohn anomaly as near the Brillouin zone boundary at the M-point. The Raman spectra, as shown for a range of temperatures below 130 K in Figure 14a, were measured by using 515 nm excitation.

To understand some of the modes, the group turned to Lee et al., who predicted the appearance of two different modes in a 1D metal in a CDW state: an amplitude mode (amplitudon) and a phase mode (phason) [147]. The phase mode is a vibration representing the electron density wave in an atomic lattice which has been rearranged (whereas a phonon concerns the translation of atomic positions), and the amplitude mode is a vibration of the ions resulting in an oscillation of the intensity of the charge density and the magnitude of the CDW gap. The amplitude and phase modes are best identified by their frequency shifts, intensities, and damping rates.

It is this behavior of narrowing and intensifying of the labeled Amp 1 and Amp 2 modes with decreasing temperature that reveals them as CDW amplitude modes. As the temperature decreases, the intensity of the labeled P1 and P2 modes increases more rapidly than the intensity of the amplitude modes, but, otherwise, the frequencies and full width at half maximum do not vary much with temperature. This observation reveals the peaks to be phase modes, which are observed only in the C-CDW state, because, while in the IC-CDW state, they have only acoustic (not optical) dispersions and are therefore not Raman active. Figure 14c shows the atomic vibration of the amplitude and phase modes at an electronic temperature of 10 K. The most notable vibration of the group is one of the amplitude modes, which allows the Se atoms to form a circular group vibration.

Chowdhury et al., used first-principles calculations to probe the effects of mechanical strain on the magnetic and optical properties of monolayer 2*H*-$TaSe_2$ [148]. Unexpected spin behaviors were predicted, such as uniaxial-strain-induced ferromagnetism and *E* phonon degeneracy lifting, mainly due to the nuanced dependence of such properties on strain. For the first unexpected behavior, their calculations showed that any magnetic properties depended on the exchange within the 5*d* orbitals of the Ta atoms. As for the effects of strain on Raman-active phonon modes, it was found that the *E* phonon degeneracy was lifted, and any electron–phonon interactions depended on the strain and its direction. These calculations revealed that CDWs weakened the magnetic properties due to symmetry breaking and Ta atom displacements. Overall, such calculations could be applicable to other CDW 2D materials.

In addition to work on 2*H*-$TaSe_2$, the 1*T* phase has also had its share of academic pursuits. One example is with Wang et al. [149], who look at the temperature-dependent Raman spectra and phonon frequencies of 6.3 nm– and 3 nm–thick 1*T*-$TaSe_2$ (whose data are shown in Figure 15). For the thinner sample, both C-CDW soft modes are observed and follow the same evolution as observed in the thicker sample. Furthermore, they remain observable up to higher temperatures compared with the thicker case. The recovery of the C-CDW state in the cooling cycle suggests that no deterioration took place at high temperatures (585 K). Moreover, based on the frequencies of the soft modes, the C-IC

phase transition temperatures were determined to be 520 and 570 K for thicker and thinner 1*T*-$TaSe_2$ samples, respectively.

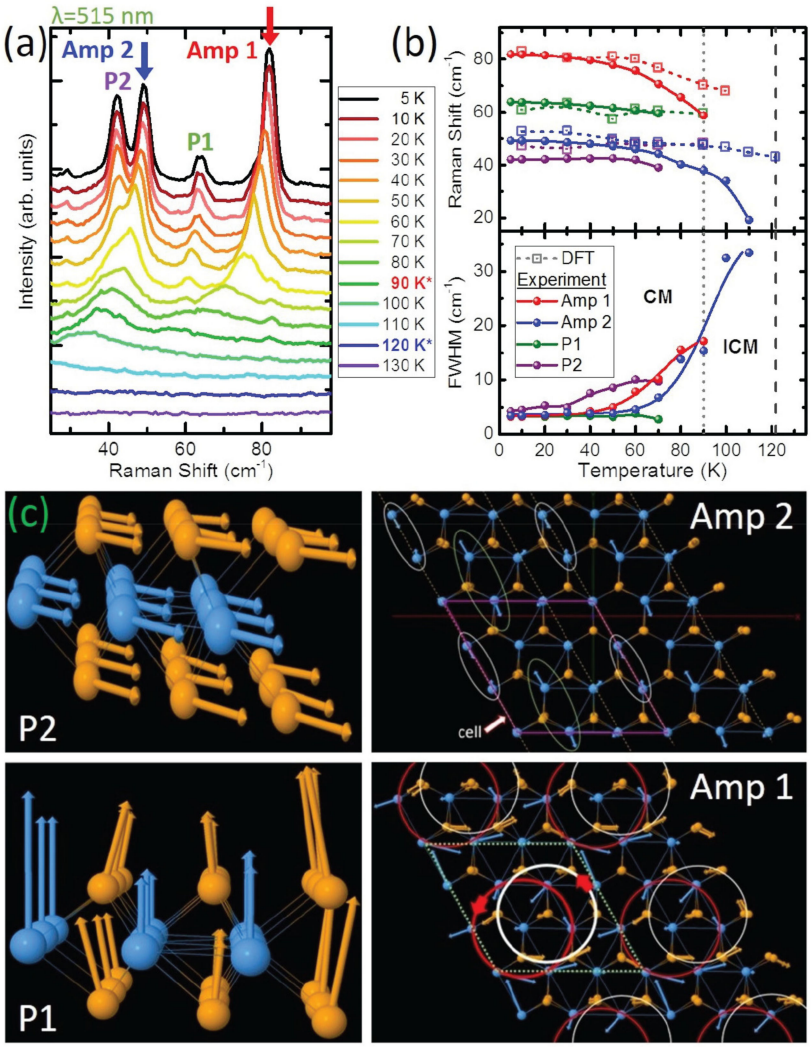

Figure 14. (**a**) Low-frequency Raman spectra show four modes emerge at low temperatures: Amp 1, Amp 2, P1, and P2. Amp 1 and Amp 2 are the CDW amplitude modes, whereas P1 and P2 are the phase modes. The transition temperature for the IC- (C-) phase is indicated in the legend by the blue (red) star. (**b**) Temperature dependence of the frequencies and full width at half maximum of Amp 1, Amp 2, P1, and P2. The DFT-calculated frequencies are plotted as a function of electronic temperature, using the same temperature axis. Solid lines guide the eye. The transition temperature for the IC-CDW (C-CDW) is indicated by a dark (light) gray dashed line. (**c**) DFT-calculated vibrations for the phase (side view) and amplitude (top view) modes. Reprinted figure with permission from Reference [108]. Copyright 2019 by the American Physical Society.

Similar work surrounding transition temperatures was performed by Samnakay et al. [127]. They found that the sample thickness required for inducing transition temperature changes is similar to the length of the phonon mean free path, as supported by observed modifications in the phonon spectrum of thin films as compared to bulk ones [150]. Because different CDW materials have different phase diagrams, thickness-dependence trends observed for one material are not readily transferrable to another. They refer to other work, wherein a super-cooled state in nm thick 1*T*-TaS_2 resulted from rapid sample cooling, and this was indicative of C-CDW suppression [151]. Thus, for $TaSe_2$, the observed thickness dependence of the phase transition temperature was able to be interpreted qualitatively within their physical model. By defining the phase-transition temperature as the balance

between the energy for elastic periodic lattice distortions and the energy reduced after a phase transition to the new CDW ground state, one may conclude with ease that any observed changes due to film thickness are unique to each material.

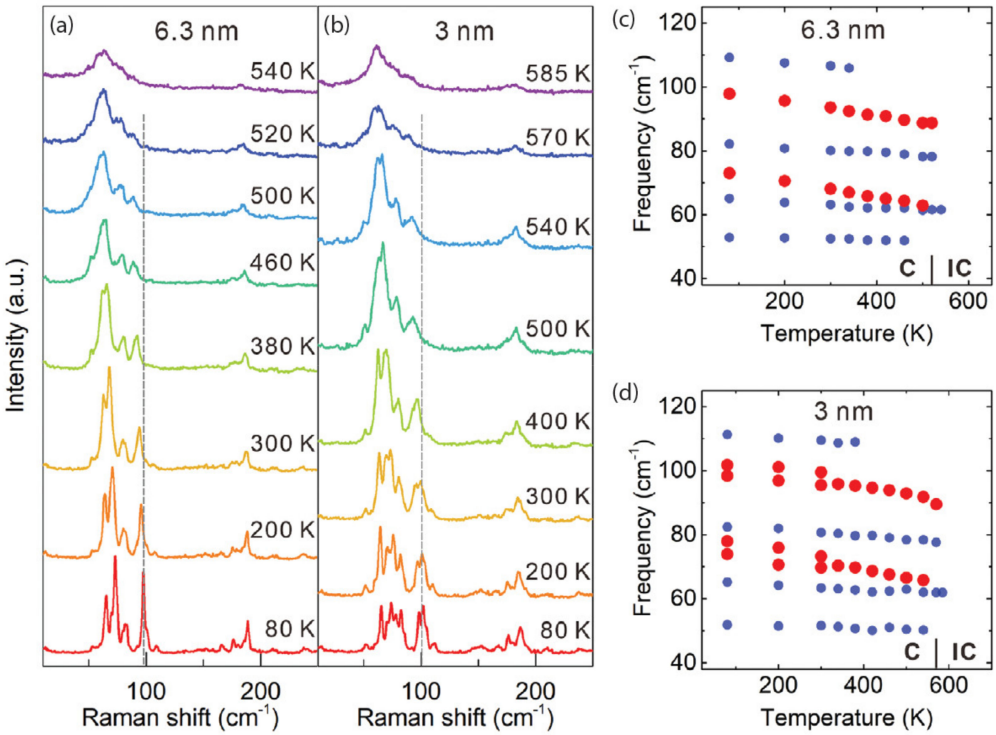

Figure 15. Raman spectroscopic investigation of the CDW transition in 6.3 nm– and 3 nm–thick 1*T*-$TaSe_2$. Raman spectra are shown for (**a**) 6.3 nm and (**b**) 3 nm 1*T*-$TaSe_2$ at selected temperatures for the heating cycle. The temperature dependence of the phonon frequencies is shown for the (**c**) 6.3 nm and (**d**) 3 nm 1*T*-$TaSe_2$. Soft modes are indicated with red dots. Reprinted figure with permission from Reference [149]. Copyright 2020 by John Wiley and Sons, Inc.

For these reasons, which extend to most 2D materials, there is a thickness dependence of the phase-transition temperature that can increase or decrease depending on the material as its film thickness is modified. Moreover, though the exact mechanism that causes this phenomenon is a point of debate, the idea that confinement and dimensionality have drastic effects on CDW-exhibiting materials, such as TaS_2 and $TaSe_2$, is well established.

5. Effects of Confinement and Dimensionality

Since applications for quantum devices often require samples to be exfoliated from or grown into few-layer material, the heavy contributions by phenomena such as vdW interactions to layer-dependent properties warrant careful treatment in calculations. This section focuses on the effects of confinement and dimensionality, which can manifest frequently as comparisons between monolayer, few-layer, and bulk systems, both in computational methods and experimental data.

5.1. Confinement and Dimensionality in TaS_2

Some interesting observations can be made when a CDW-exhibiting material is forced into confinement with another adjacent material. Yamada et al., looked at bismuth ultrathin films on 1*T*-TaS_2 and investigated electronic states with ARPES and first-principles band-structure calculations [118,152]. Though some ARPES work has been shown earlier [118], this work explores the CDW proximity effect. It was then found that the film on 1*T*-TaS_2 underwent a major structural transition from (111) to (110) upon reducing the thickness, and the observation was accompanied by changes in the energy band structure. They go

on to discuss the mechanisms for those observations. An example of these ARPES data and band structure calculations are shown in Figure 16.

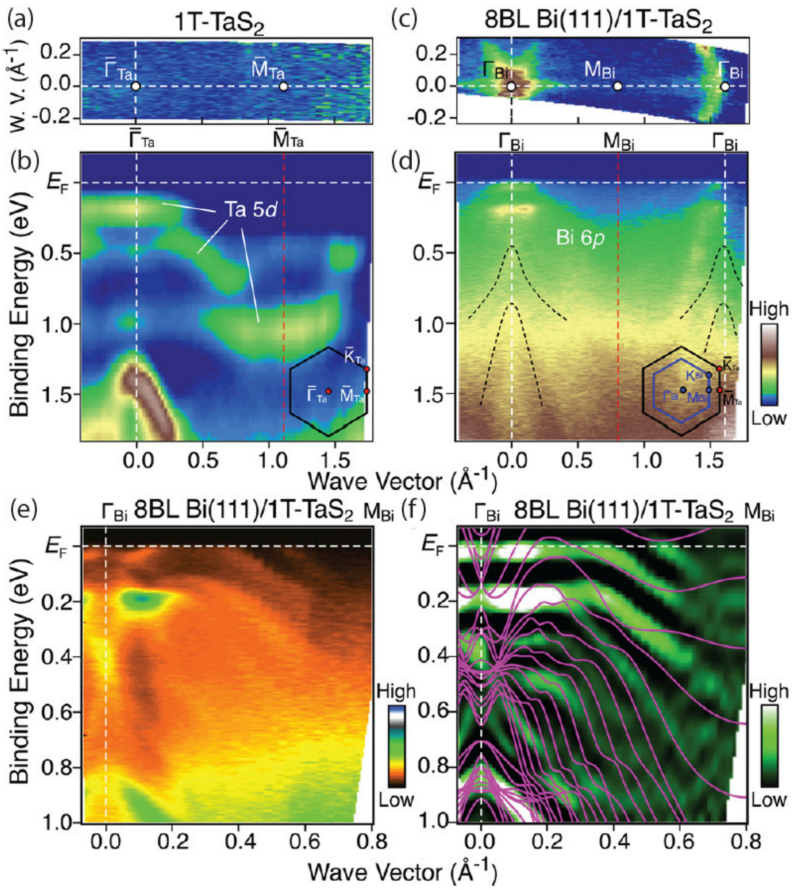

Figure 16. (**a**) Plot of ARPES intensity at the Fermi energy is shown for pristine 1*T*-TaS_2 as a function of in-plane wave vector. (**b**) ARPES intensity as a function of binding energy. (**c**,**d**) Show the same content as (**a**,**b**) but for 8BL Bi(111) on 1*T*-TaS_2. (**e**,**f**) Shows ARPES data and their second derivative intensities, respectively, for 8BL Bi(111)/1*T*-TaS_2 as a function of binding energy and wave vector. Solid curves in (**f**) are calculated band dispersions for free-standing 8BL Bi(111). The ARPES data were recorded at 30 K. Reprinted with permission from Reference [152]. Copyright 2018 by the American Chemical Society.

Other groups have explored coexisting states, such as Yang et al. [153]. TMDs with both CDW and superconducting orders can offer ideal platforms for exploring the effects of dimensionality on correlated electronic phases. According to the authors, dimensionality has a large effect on superconductivity and CDW instabilities. They report enhancement of the superconducting transition temperature from sub-Kelvin temperatures in bulk to 3.4 K for monolayer 2*H*-TaS_2. It is also found that the transport signature of a CDW phase transition vanishes as one approaches monolayer thicknesses. It is shown that the root cause for the enhancement stems from a reduction of the CDW amplitude, resulting in a substantial increase of the DOS at the Fermi energy. This competition between CDW and superconductivity as one approaches the 2D limit offers deep insights in our understanding of correlated electronic phases in reduced dimensions. Similar topical work has explored the relationship between CDWs and superconductivity [154,155]. Castro Neto proposed that, because of the strong variations in electron–phonon coupling, as well as imperfect nesting of the Fermi surface, the CDW gap is six-fold symmetric. Ultimately, such a configuration leads to the reduction of electron–phonon scattering. Since lattice inversion symmetry is lost during the CDW phase, Dirac electrons become coupled to acoustic phonons, leading to a

damping of the Dirac electrons. Lastly, these phonons drive the system to a superconducting state via a Kosterlitz–Thouless phase transition [154]. Koley et al. [155], on the other hand, looked to understand the competition between CDW and superconducting states by adding nonmagnetic disorder to them. Both random disorder and clustered disorder were explored by using a self-consistent Bogoliubov–de Gennes formulation. Theoretical observations of the evolution of both states were made by using a Monte Carlo method [155].

Some works surrounding the effects of confinement or dimensionality focus on the layer-by-layer response of the material. For instance, Ishiguro et al., report a layer-dependence study centered on the transition between the IC-CDW and NC-CDW and utilized electrical resistance measurements and Raman spectroscopy [156]. It was found that temperature hysteresis decreases in this transition as the number of layers decreases, and this observation is in contrast to the C-CDW and NC-CDW transition. This hysteresis trend being different for these two types of transitions was explained by the difference in the CDW superstructure along the out-of-plane direction between the C-CDW and IC-CDW phases.

Kuhn et al., found that, even though 1*T*-TaS_2 is a conventional 2D material, isotropic 3D charge transfer mechanisms appear in the C-CDW phase, indicating strong coupling between layers [157]. To observe and understand this oddity of dimensionality, they use a unique experimental approach and DFT to specifically probe how ultrafast charge transfer takes on a 3D or 2D character, depending on the circumstances. The experimental data are collected by what is known as the X-ray spectroscopic core–hole–clock method, which enables the experimenter to prepare in- and out-of-plane polarized sulfur 3*p* orbital occupation (with respect to the plane of 1*T*-TaS_2) for monitoring sub-fs wave-packet delocalization. The details for some of their work are shown in Figure 17.

For this study, DFT was implemented via the Siesta code and used to compute the electronic structure of 1*T*-TaS_2 in the C-CDW phase [158]. The calculations used the vdW-DF by Dion et al. [117] with the optimized exchange from the work of Klimes et al. [159]. Ultimately, the theory shows that interlayer interactions in the C-CDW phase cause isotropic 3D charge transfer as opposed to layer-stacking variations, and this mechanism for phase transitions is applicable to other CDW materials. In the case of TaS_2, the projected DOS is distributed over a wide energy range, reflecting the covalent bonding with neighboring atoms in the material, and observations have been made via inverse photoemission experiments [160,161].

5.2. Confinement and Dimensionality in $TaSe_2$

When talking about confinement and dimensionality in $TaSe_2$, some similar conclusions may be drawn from material behaviors as one approaches the 2D limit. Yan et al., talk about the band dispersions for bulk 2*H*-$TaSe_2$ and 1*T*-$TaSe_2$ and describe what happens as the dimension is reduced from 3D to 2D [82]. Electrons in monolayer $TaSe_2$ become confined into the plane, offering a genuine 2D character to the electronic structure. However, as one could surmise from the earlier case of TaS_2, one may also expect that the reduced dimensionality alters the Fermi surface topology, and this alteration implies that CDW transitions are subject to dimensionality effects.

Other work, such as the ones from Chowdhury et al. [162,163], looked to learn more about how these dimensionality and confinement effects contribute to structural formation and, more specifically, to the formation of CDW states. Though various efforts have been made, many making observations or calculations that directly involve the effect of vdW interactions and reduced dimensionality on the CDW phase [164,165], the level of detail was still lacking as far as how exactly a CDW state formed as a function of layer number. In summary, 2D systems formed triangular structures and bulk systems formed striped structures while in the C-CDW phase. The 2D case reflected the lack of presence of long-range order along the *z*-axis normally attributable to vdW interactions. Thus, naturally, the bulk case can yield a striped structure with decreasing temperature, because of the presence of long-range order.

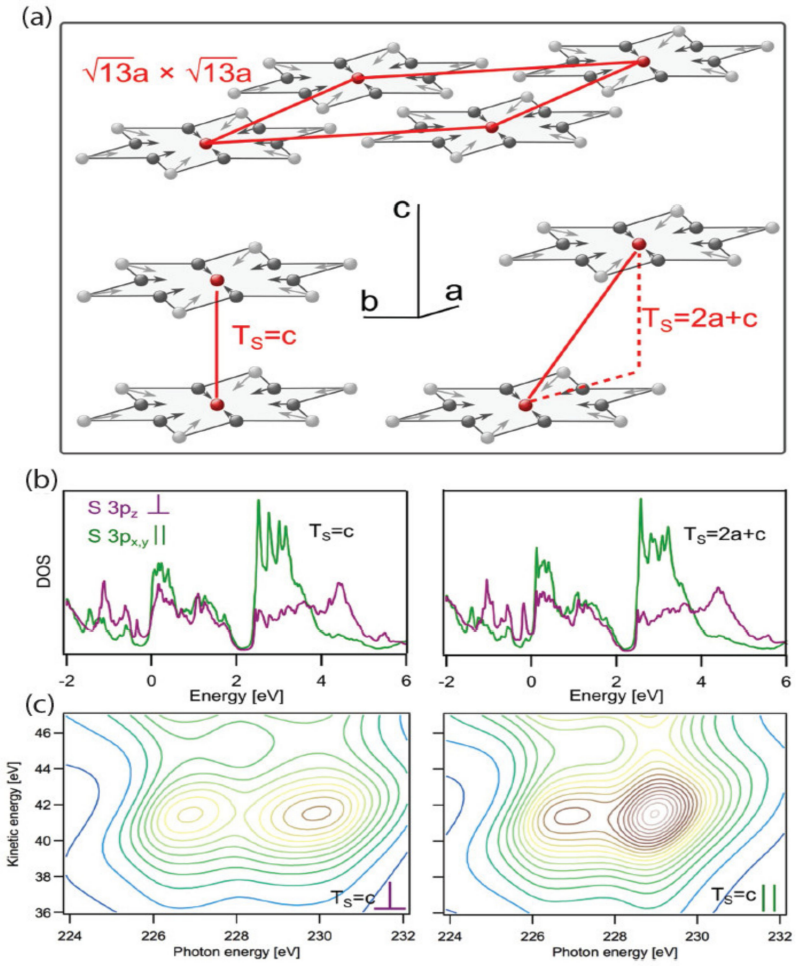

Figure 17. DFT calculations of the electronic structure and spectral signatures of 1*T*-TaS_2 are shown for two C-CDW interlayer stacking arrangements. (**a**) The 13 *a* × 13 *a* Star-of-David reconstruction of the Ta layers is illustrated. All atoms of each star are displaced (depicted with arrows) toward the center atom. Bottom left: CDW stacking of the Ta planes with the Star-of-David centers on top of each other (T_s = c). Bottom right: CDW stacking with a stacking vector having an in-plane component (T_s = 2a + c). (**b**) DFT calculations of the PDOS of the polarized S 3*p* states with on-site S 2*s* core hole for T_s = c (**left**) and T_s = 2a + c (**right**). Purple shows the out-of-plane PDOS, and green shows the in-plane PDOS. The Fermi level is located at 0 eV. (**c**) Simulations of the sulfur scattering planes based on the PDOS from (**b**). Intensity increases from blue to brown. Reference [157] is an open-access article distributed under the terms of the Creative Commons CC BY (available online at https://creativecommons.org/licenses/ (accessed on 14 December 2021)) license, which permits unrestricted use, distribution, and reproduction in any medium.

Chowdhury et al., expanded the work to address the natural question of whether or not the presence of interacting neighboring layers affects these ground state structural formations and whether there is a coherent layer-dependence that can link the two extreme cases of 1L and bulk. They used DFT to investigate the 2L, 3L, 4L, 5L, and 6L cases, with all cases starting from the same type of super-cells as built for 1L and bulk, and with all cases being examined as the electronic temperature was reduced from 300 to 10 K.

Sometimes confined systems, such as these 2D CDW materials, are subjected to conditions that may bring about a 3D-like nature. Such was the case in Ji et al. [166], who reported on the optical suppression of the C-CDW over a sub-ps timescale. The group claims that the short timescales involved in establishing the stacking order implies that the nucleation of the IC-CDW phase is inherently of a 3D nature. The energy of the optically excited electronic state dissipates energy into modes representing periodic lattice distortions

through strong electron–phonon coupling. Some of their theoretical approach is depicted in Figure 18. Overall, their results highlight the importance of considering the 3D nature of CDWs for $TaSe_2$ and related materials. Corresponding band structure and joint DOS calculations were performed by using the ELK code [167].

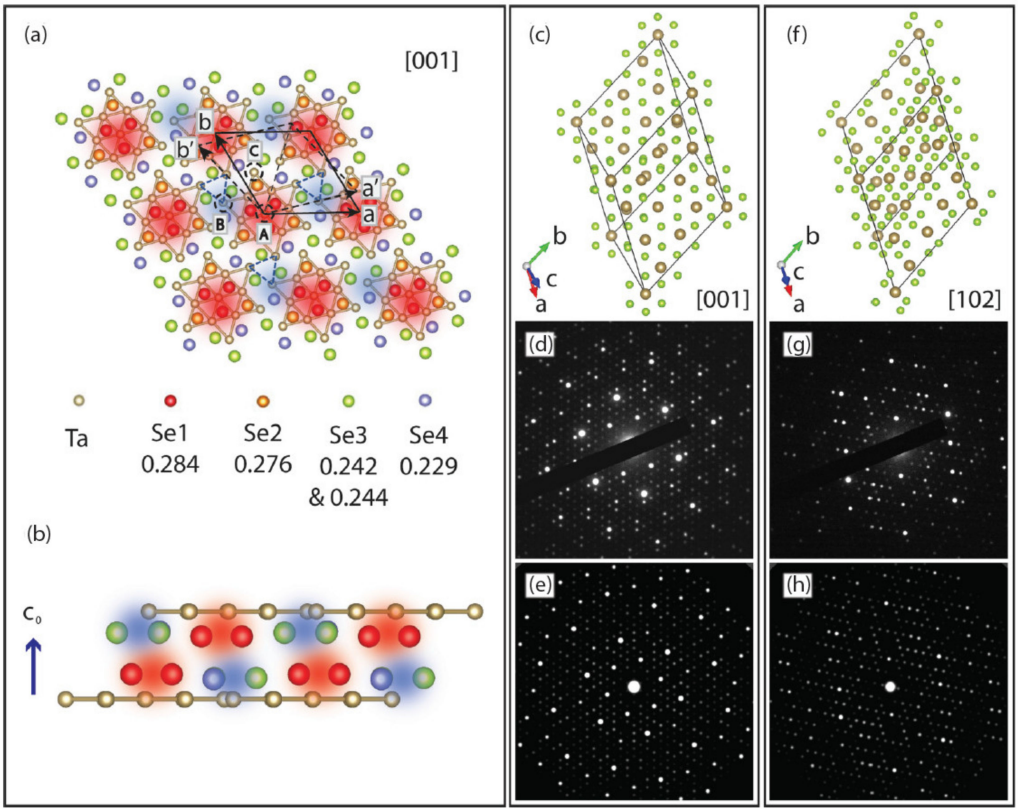

Figure 18. (**a**) Illustration of superstructure and stacking arrangement in 1*T*-$TaSe_2$. The periodic lattice displacements form a 13-Ta-atom Star-of-David cluster (solid bonds). Blue dashed triangles indicate the threefold symmetric stacking displacements. Se atoms are color coded according to their *c*-axis coordinate (in fractions of *c*), as listed in the lower part of (**a**). The Se atoms at the center of a Star-of-David cluster are at highest (most protruding, red-shaded areas) positions, whereas other Se atoms at the lowest positions are shown as blue-shaded areas. (**b**) Stacking arrangement along the c_0 direction for two adjacent layers of the C-CDW phase. Projections of the C-CDW phase at (**c**) [001] and (**f**) [102] zone axis are shown with the corresponding experimental diffraction patterns in (**d**) and (**g**), respectively. The simulated diffraction patterns are shown along [001] (**e**) and [102] (**h**). Reference [166] is an open-access article distributed under the terms of the Creative Commons CC BY (https://creativecommons.org/licenses/ (accessed on 14 December 2021)) license, which permits unrestricted use, distribution, and reproduction in any medium.

Lastly, a general framework for dimensionality dependent CDWs in both TaS_2 and $TaSe_2$ was proposed by Lin et al. [168]. They focused on 2*H*-MX_2 (M = Nb, Ta and X = S, Se). One of the key takeaways in the context of dimensionality comes from their description of how ionic charge transfer, electron–phonon coupling, and the spatial extension of the electronic wave functions contribute to CDW ordering and its thickness dependence. These three parameters were used to create a unified phase diagram describing instabilities in low-dimensional limits. This diagram is illustrated in Figure 19c. As can be seen, the interplay between these three parameters is expected to form an abyss-like shape, deepening at regions with low ionic charge transfer and electron–phonon coupling, as well as high spatial extensions. Above the surface of the resulting terrain is a parameter space within

which the CDW is forbidden. Below this space, the CDW is allowed to emerge and does so for some of the example materials.

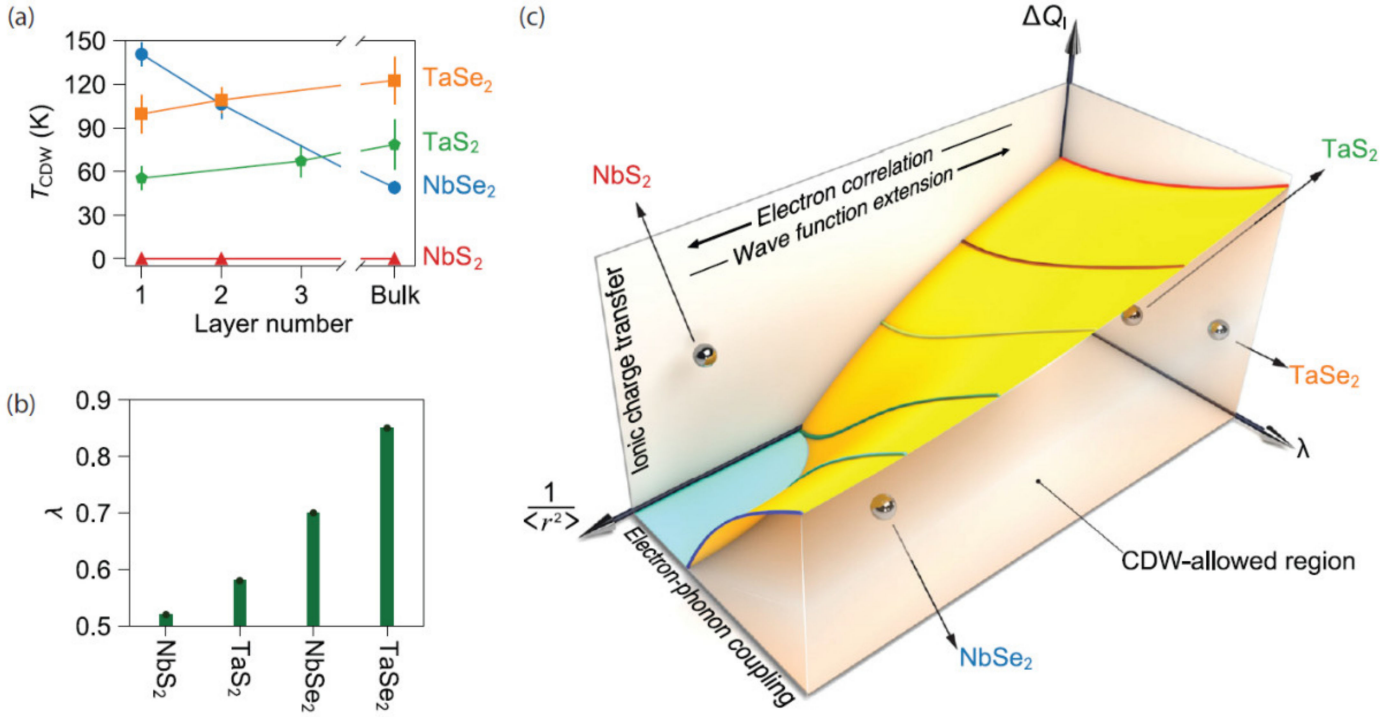

Figure 19. (**a**) Thickness dependence of the CDW transition temperature in 2*H*-MX_2. Error bars are standard deviations obtained from the least-squares fits to the temperature-dependent amplitude mode intensity. (**b**) The calculated values of electron–phonon coupling constant (λ) for monolayer 1*H*-MX_2. (**c**) Schematic illustration of the possible phase diagram describing the CDW response in a layered material in terms of ionic charge transfer (ΔQ_I), electron–phonon coupling constant (λ), and the spatial extension of electronic wave functions ($1/\langle r^2 \rangle$). Reference [168] is an open-access article distributed under the terms of the Creative Commons CC BY license (Available online: https://creativecommons.org/licenses/ (accessed on 14 December 2021)), which permits unrestricted use, distribution, and reproduction in any medium.

6. Future Outlook and Conclusions

Some key takeaways in this work show that even materials exhibiting similar band structures, such as $TaSe_2$ and TaS_2, have considerable differences. For instance, TaS_2 has a more pronounced non-commensurate transition between room temperature and its CDW phase, whereas $TaSe_2$ does not. Furthermore, inspecting the phase diagrams of the many works presented herein will reveal that TaS_2 will form clusters of Star-of-David regions as the CDW phase is warmed, and such clusters do not form with $TaSe_2$. Rather, curvilinear regions resembling a grain boundary appear. In terms of vibrational properties, the IC-CDW phase more pronounced in $TaSe_2$ more greatly affects Raman mode observations between room temperature and temperatures corresponding to the C-CDW phase transition. In terms of dimensionality, a key point is that both materials differ significantly on their calculated electron–phonon coupling constant [168], and since such coupling is tied to superconductivity, it follows that observations of the latter would also be substantially altered.

It has become clear that computational methods, such as DFT, have resulted in wide-ranging examinations of various material systems exhibiting CDWs, and such systems have the potential to become building blocks for multifaceted quantum information platforms. It is also clear that many of these material systems are slowly becoming more available for computing applications. A future roadmap for these materials and applications involves a

successful identification and validation of certain TMDs that will most likely support such applications. A close coupling between theoretical and experimental efforts will ensure that existing data on these material platforms are used to iteratively guide the construction of appropriate models for newer devices, thus greatly accelerating device optimization.

Likewise, subsequent experimental verification of newer models should further advance the fabrication of an improved generation of TMD devices for experimental characterization, closing the feedback loop between theory and experiment. This cycling will greatly accelerate the fundamental understanding of CDWs in these materials, as well as the limitations one may expect in their applications. Future computing demands may involve more complex systems or defect behavior, and such modeling will eventually require the development of new computational workflows and substantial computational resources.

It must also be understood that these endeavors contain inherent risk in terms of applicability, so risks must be considered and mitigated in order to reach these promising technical goals. Because the space of all TMD materials is rather large, some candidate materials may go unexplored or be assessed too soon as being not viable. Additionally, the computational methodology may need to be adequately improved to most accurately describe the key interactions taking place in these layered materials physics. Regardless of the limitations, the ongoing interplay between theoretical and experimental efforts will be vital for continued success.

This field has greatly expanded over the decades, and much has been learned about the computational efforts surrounding CDWs in 2D materials, along with some important experiments that helped validate those computational methods. We have covered several relevant, theory-driven subtopics for TaS_2 and $TaSe_2$ including the general computational techniques and methods, atomic structures, Raman modes, and effects of confinement and dimensionality. Through understanding how the computational methods have enabled incredible advancements in quantum materials, one may anticipate the ever-expanding directions available for continued pursuit as the field brings us into the next decade.

Author Contributions: Conceptualization, methodology, and software, S.C. and F.T.; validation, A.F.R., P.V., H.M.H. and A.R.H.W.; formal analysis and investigation, S.C., A.F.R., P.V. and H.M.H.; resources, A.R.H.W. and F.T.; data curation and writing—original draft preparation, S.C. and A.F.R.; writing—review and editing, S.C., A.F.R., P.V., H.M.H., A.R.H.W. and F.T.; visualization, supervision, project administration, and funding acquisition, A.R.H.W. and F.T. All authors have read and agreed to the published version of the manuscript.

Funding: The APC was funded by the National Institute of Standards and Technology. P.M.V. acknowledges support from the National Science Foundation (NSF) under Grant Nos. DMR-1847782 and from the George Mason University Quantum Science and Engineering Center. Work presented herein was performed, for a subset of the authors, as part of their official duties for the United States Government. Funding is hence appropriated by the United States Congress directly.

Data Availability Statement: The data from new figures are available on reasonable request from the corresponding author. Data from other publishers are not available from the corresponding author of this work but may be available by reaching the corresponding author of the cited work.

Acknowledgments: Commercial equipment, instruments, software, and other materials are identified in this paper in order to specify the experimental procedure adequately. Such identification is not intended to imply recommendation or endorsement by the National Institute of Standards and Technology or the United States government, nor is it intended to imply that the materials or equipment identified are necessarily the best available for the purpose. P.M.V. acknowledges support from the National Science Foundation (NSF) under Grant Nos. DMR-1847782 and from the George Mason University Quantum Science and Engineering Center.

Conflicts of Interest: The authors declare no conflict of interest. The funders had no role in the design of the study; in the collection, analyses, or interpretation of data; in the writing of the manuscript; or in the decision to publish the results.

References

1. Chhowalla, M.; Jena, D.; Zhang, H. Two-dimensional semiconductors for transistors. *Nat. Rev. Mater.* **2016**, *1*, 16052. [CrossRef]
2. Mannix, A.J.; Kiraly, B.; Hersam, M.C.; Guisinger, N.P. Synthesis and chemistry of elemental 2D materials. *Nat. Rev. Chem.* **2017**, *1*, 0014. [CrossRef]
3. Novoselov, K.S.; Geim, A.K.; Morozov, S.; Jiang, D.; Katsnelson, M.I.; Grigorieva, I.; Dubonos, S.; Firsov, A.A. Two-dimensional gas of massless Dirac fermions in graphene. *Nature* **2005**, *438*, 197. [CrossRef] [PubMed]
4. Novoselov, K.S.; Geim, A.K.; Morozov, S.; Jiang, D.; Zhang, Y.; Dubonos, S.V.; Grigorieva, I.; Firsov, A.A. Electric field effect in atomically thin carbon films. *Science* **2004**, *306*, 666–669. [CrossRef]
5. Fröhlich, H. On the theory of superconductivity: The one-dimensional case. *Proc. R. Soc. Lond. A* **1954**, *223*, 296–305.
6. Thorne, R.E. Charge-density-wave conductors. *Phys. Today* **1996**, *49*, 42–48. [CrossRef]
7. Liu, G.; Debnath, B.; Pope, T.R.; Salguero, T.T.; Lake, R.K.; Baladin, A.A. A charge-density-wave oscillator based on an integrated tantalum disulfide–boron nitride–graphene device operating at room temperature. *Nat. Nanotechnol.* **2016**, *11*, 845–850. [CrossRef]
8. Gruner, G. *Density Waves in Solids*; Perseus Publishing: New York, NY, USA, 2000.
9. Wilson, J.A.; Di Salvo, F.J.; Mahajan, S. Charge-density waves and superlattices in the metallic layered transition metal dichalcogenides. *Adv. Phys.* **1975**, *24*, 2. [CrossRef]
10. Wilson, J.A.; Yoffe, A.D. The transition metal dichalcogenides discussion and interpretation of the observed optical, electrical and structural properties. *Adv. Phys.* **1969**, *18*, 73. [CrossRef]
11. Sipos, B.; Kusmartseva, A.F.; Akrap, A.; Berger, H.; Forró, L.; Tutis, E. From Mott state to superconductivity in 1*T*-TaS_2. *Nat. Mater.* **2008**, *7*, 960. [CrossRef]
12. McMillan, W.L. Theory of discommensurations and the commensurate-incommensurate charge-density-wave phase transition. *Phys. Rev. B* **1976**, *14*, 1496. [CrossRef]
13. Rice, T.M.; Scott, G.K. New mechanism for a charge-density-wave instability. *Phys. Rev. Lett.* **1975**, *35*, 120. [CrossRef]
14. Hirsch, J.E. Charge-density-wave to spin-density-wave transition in the extended Hubbard model. *Phys. Rev. Lett.* **1984**, *53*, 2327. [CrossRef]
15. Tucker, J.R.; Lyons, W.G.; Gammie, G. Theory of charge-density-wave dynamics. *Phys. Rev. B* **1988**, *38*, 1148. [CrossRef] [PubMed]
16. Efetov, K.B.; Larkin, A.I. Charge-density wave in a random potential. *Sov. Phys. JETP* **1977**, *45*, 2350–2361.
17. Sugai, S. Lattice vibrations in the charge-density-wave states of layered transition metal dichalcogenides. *Phys. Status Solidi B Basic Res.* **1985**, *129*, 13–39. [CrossRef]
18. Zettl, A.; Grüner, G. Charge-density-wave dynamics in TaS_3. *Phys. Rev. B* **1982**, *25*, 2081. [CrossRef]
19. Stoffel, N.G.; Kevan, S.D.; Smith, N.V. Experimental band structure of 1*T*-$TiSe_2$ in the normal and charge-density-wave phases. *Phys. Rev. B* **1985**, *31*, 8049. [CrossRef]
20. Jacobs, A.E.; Walker, M.B. Phenomenological theory of charge-density-wave states in trigonal-prismatic, transition-metal dichalcogenides. *Phys. Rev. B* **1980**, *21*, 4132. [CrossRef]
21. Thompson, A.H.; Zettl, A.; Grüner, G. Charge-Density-Wave Transport in TaS_3. *Phys. Rev. Lett.* **1981**, *47*, 64. [CrossRef]
22. Grüner, G.; Zawadowski, A.; Chaikin, P.M. Nonlinear conductivity and noise due to charge-density-wave depinning in $Nbse_3$. *Phys. Rev. Lett.* **1981**, *46*, 511. [CrossRef]
23. Monceau, P.; Richard, J.; Renard, M. Interference Effects of the Charge-Density-Wave Motion in $NbSe_3$. *Phys. Rev. Lett.* **1980**, *45*, 43. [CrossRef]
24. Su, W.P.; Schrieffer, J.R. Fractionally charged excitations in charge-density-wave systems with commensurability 3. *Phys. Rev. Lett.* **1981**, *46*, 738. [CrossRef]
25. Grüner, G.; Zettl, A. Charge density wave conduction: A novel collective transport phenomenon in solids. *Phys. Rep.* **1985**, *119*, 117–232. [CrossRef]
26. Tsutsumi, K.; Takagaki, T.; Yamamoto, M.; Shiozaki, Y.; Ido, M.; Sambongi, T.; Yamaya, K.; Abe, Y. Direct Electron-Diffraction Evidence of Charge-Density-Wave Formation in $NbSe_3$. *Phys. Rev. Lett.* **1977**, *39*, 1675. [CrossRef]
27. Bak, P.; Mukamel, D.; Villain, J.; Wentowska, K. Commensurate-incommensurate transitions in rare-gas monolayers adsorbed on graphite and in layered charge-density-wave systems. *Phys. Rev. B* **1979**, *19*, 1610. [CrossRef]
28. Chen, C.H.; Gibson, J.M.; Fleming, R.M. Direct Observation of Charge-Density-Wave Discommensurations and Dislocations in 2*H*-$TaSe_2$. *Phys. Rev. Lett.* **1981**, *47*, 723. [CrossRef]
29. Moncton, D.E.; Axe, J.D.; DiSalvo, F.J. Neutron scattering study of the charge-density wave transitions in 2*H*-$TaSe_2$ and 2*H*-$NbSe_2$. *Phys. Rev. B* **1977**, *16*, 801. [CrossRef]
30. Fukuyama, H.; Lee, P.A. Dynamics of the charge-density wave, Impurity pinning in a single chain. *Phys. Rev. B* **1978**, *17*, 535. [CrossRef]
31. Harper, J.M.; Geballe, T.H.; DiSalvo, F.J. Thermal properties of layered transition-metal dichalcogenides at charge-density-wave transitions. *Phys. Rev. B* **1977**, *15*, 2943. [CrossRef]
32. Yoshioka, D.; Fukuyama, H. Charge density wave state of two-dimensional electrons in strong magnetic fields. *J. Phys. Soc. Jpn.* **1979**, *47*, 394–402. [CrossRef]
33. Yoshioka, D.; Lee, P.A. Ground-state energy of a two-dimensional charge-density-wave state in a strong magnetic field. *Phys. Rev. B* **1983**, *27*, 4986. [CrossRef]

34. Scalettar, R.T.; Bickers, N.E.; Scalapino, D.J. Competition of pairing and Peierls–charge-density-wave correlations in a two-dimensional electron-phonon model. *Phys. Rev. B* **1989**, *40*, 197. [CrossRef]
35. Carpinelli, J.M.; Weitering, H.M.H.; Plummer, E.W.; Stumpf, R. Direct observation of a surface charge density wave. *Nature* **1996**, *381*, 398–400. [CrossRef]
36. Koulakov, A.A.; Fogler, M.M.; Shklovskii, B.I. Charge density wave in two-dimensional electron liquid in weak magnetic field. *Phys. Rev. Lett.* **1996**, *76*, 499. [CrossRef] [PubMed]
37. Hill, H.M.; Rigosi, A.F.; Krylyuk, S.; Tian, J.; Nguyen, N.V.; Davydov, A.V.; Newell, D.B.; Hight Walker, A.F.R. Comprehensive optical characterization of atomically thin $NbSe_2$. *Phys. Rev. B* **2018**, *98*, 165109. [CrossRef] [PubMed]
38. Whangbo, M.H.; Canadell, E.; Foury, P.; Pouget, J.P. Hidden Fermi surface nesting and charge density wave instability in low-dimensional metals. *Science* **1991**, *252*, 96–98. [CrossRef] [PubMed]
39. Snow, C.S.; Karpus, J.F.; Cooper, S.L.; Kidd, T.E.; Chiang, T.C. Quantum Melting of the Charge-Density-Wave State in 1*T*-$TiSe_2$. *Phys. Rev. Lett.* **2003**, *91*, 136402. [CrossRef]
40. Thomson, R.E.; Burk, B.; Zettl, A.; Clarke, J. Scanning tunneling microscopy of the charge-density-wave structure in 1*T*-TaS_2. *Phys. Rev. B* **1994**, *49*, 16899. [CrossRef]
41. Rossnagel, K.; Rotenberg, E.; Koh, H.; Smith, N.; Kipp, L. Fermi surface, charge-density-wave gap, and kinks in 2*H*-$TaSe_2$. *Phys. Rev. B* **2005**, *72*, 121103. [CrossRef]
42. Valla, T.; Fedorov, A.V.; Johnson, P.D.; Xue, J.; Smith, K.E.; Di Salvo, F.J. Charge-density-wave-induced modifications to the quasiparticle self-energy in 2*H*-$TaSe_2$. *Phys. Rev. Lett.* **2000**, *85*, 4759. [CrossRef]
43. Gweon, G.H.; Denlinger, J.D.; Clack, J.A.; Allen, J.W.; Olson, C.G.; DiMasi, E.; Aronson, M.C.; Foran, B.; Lee, S. Direct observation of complete Fermi surface, imperfect nesting, and gap anisotropy in the high-temperature incommensurate charge-density-wave compound $SmTe_3$. *Phys. Rev. Lett.* **1998**, *81*, 886. [CrossRef]
44. Shen, D.W.; Xie, B.P.; Zhao, J.F.; Yang, L.X.; Fang, L.; Shi, J.; He, R.H.; Lu, D.H.; Wen, H.M.H.; Feng, D.L. Novel mechanism of a charge density wave in a transition metal dichalcogenide. *Phys. Rev. Lett.* **2007**, *99*, 216404. [CrossRef] [PubMed]
45. Johannes, M.D.; Mazin, I.I.; Howells, C.A. Fermi-surface nesting and the origin of the charge-density wave in $NbSe_2$. *Phys. Rev. B* **2006**, *73*, 205102. [CrossRef]
46. Calandra, M.; Mazin, I.I.; Mauri, F. Effect of dimensionality on the charge-density wave in few-layer 2*H*-$NbSe_2$. *Phys. Rev. B* **2009**, *80*, 241108. [CrossRef]
47. Ge, Y.; Liu, A.Y. Effect of dimensionality and spin-orbit coupling on charge-density-wave transition in 2*H*-$TaSe_2$. *Phys. Rev. B* **2012**, *86*, 104101. [CrossRef]
48. Head-Marsden, K.; Flick, J.; Ciccarino, C.J.; Narang, P. Quantum Information and Algorithms for Correlated Quantum Matter. *Chem. Rev.* **2020**, *121*, 3061–3120. [CrossRef] [PubMed]
49. Kabiraj, A.; Mahapatra, S. Machine-Intelligence-Driven High-Throughput Prediction of 2D Charge Density Wave Phases. *J. Phys. Chem. Lett.* **2020**, *11*, 6291–6298. [CrossRef]
50. Ugeda, M.M.; Bradley, A.J.; Zhang, Y.; Onishi, S.; Chen, Y.; Ruan, W.; Ojeda-Aristizabal, C.; Ryu, H.; Edmonds, M.T.; Tsai, H.-Z. Characterization of collective ground states in single-layer $NbSe_2$. *Nat. Phys.* **2016**, *12*, 92. [CrossRef]
51. Xi, X.; Wang, Z.; Zhao, W.; Park, J.-H.; Law, K.T.; Berger, H.; Forró, L.; Shan, J.; Mak, K.F. Ising pairing in superconducting $NbSe_2$ atomic layers. *Nat. Phys.* **2016**, *12*, 139. [CrossRef]
52. Xi, X.; Zhao, L.; Wang, Z.; Berger, H.; Forró, L.; Shan, J.; Mak, K.F. Strongly enhanced charge-density-wave order in monolayer $NbSe_2$. *Nat. Nanotechnol.* **2015**, *10*, 765. [CrossRef] [PubMed]
53. Soumyanarayanan, A.; Yee, M.M.; He, Y.; Van Wezel, J.; Rahn, D.J.; Rossnagel, K.; Hudson, E.W.; Norman, M.R.; Hoffman, J.E. Quantum phase transition from triangular to stripe charge order in $NbSe_2$. *Proc. Natl. Acad. Sci. USA* **2013**, *110*, 1623–1627. [CrossRef] [PubMed]
54. Weber, F.; Rosenkranz, S.; Castellan, J.-P.; Osborn, R.; Hott, R.; Heid, R.; Bohnen, K.-P.; Egami, T.; Said, A.; Reznik, D. Extended Phonon Collapse and the Origin of the Charge-Density Wave in 2*H*-$NbSe_2$. *Phys. Rev. Lett.* **2011**, *107*, 107403. [CrossRef]
55. Bianco, R.; Errea, I.; Monacelli, L.; Calandra, M.; Mauri, F. Quantum enhancement of charge density wave in NbS_2 in the two-dimensional limit. *Nano Lett.* **2019**, *19*, 3098–3103. [CrossRef] [PubMed]
56. Heil, C.; Poncé, S.; Lambert, H.; Schlipf, M.; Margine, E.R.; Giustino, F. Origin of superconductivity and latent charge density wave in NbS 2. *Phys. Rev. Lett.* **2017**, *119*, 087003. [CrossRef]
57. Leroux, M.; Le Tacon, M.; Calandra, M.; Cario, L.; Measson, M.A.; Diener, P.; Borrissenko, E.; Bosak, A.; Rodiere, P. Anharmonic suppression of charge density waves in 2*H*-NbS_2. *Phys. Rev. B* **2012**, *86*, 155125. [CrossRef]
58. Leroux, M.; Cario, L.; Bosak, A.; Rodiere, P. Traces of charge density waves in NbS_2. *Phys. Rev. B* **2018**, *97*, 195140. [CrossRef]
59. Tresca, C.; Calandra, M. Charge density wave and spin 1/2 insulating state in single layer 1*T*-NbS_2. *2D Mater.* **2019**, *6*, 035041. [CrossRef]
60. Cudazzo, P.; Müller, E.; Habenicht, C.; Gatti, M.; Berger, H.; Knupfer, M.; Rubio, A.; Huotari, S. Negative plasmon dispersion in 2*H*-NbS_2 beyond the charge-density-wave interpretation. *New J. Phys.* **2016**, *18*, 103050. [CrossRef]
61. Dolui, K.; Sanvito, S. Dimensionality-driven phonon softening and incipient charge density wave instability in TiS_2. *Europhys. Lett.* **2016**, *115*, 47001. [CrossRef]

62. Mottas, M.L.; Jaouen, T.; Hildebrand, B.; Rumo, M.; Vanini, F.; Razzoli, E.; Giannini, E.; Barreteau, C.; Bowler, D.R.; Monney, C.; et al. Semimetal-to-semiconductor transition and charge-density-wave suppression in $1T-TiSe_{2-x}-S_x$ single crystals. *Phys. Rev. B* **2019**, *99*, 155103. [CrossRef]
63. Thompson, A.H. Electron-Electron Scattering in TiS_2. *Phys. Rev. Lett.* **1975**, *35*, 1786. [CrossRef]
64. Krogel, J.T.; Yuk, S.F.; Kent, P.R.; Cooper, V.R. Perspectives on van der Waals Density Functionals: The Case of TiS_2. *J. Phys. Chem. A* **2020**, *124*, 9867–9876. [CrossRef] [PubMed]
65. Pandey, C.; Ahmed, G.; Sharma, R.; Sharma, Y. Ab initio study of anisotropic properties in isomorphic TiX_2 (X = S, Se, Te). *Int. J. Quantum Chem.* **2021**, *121*, e26575. [CrossRef]
66. Van Wezel, J.; Nahai-Williamson, P.; Saxena, S.S. Exciton-phonon-driven charge density wave in $TiSe_2$. *Phys. Rev. B* **2010**, *81*, 165109. [CrossRef]
67. May, M.M.; Brabetz, C.; Janowitz, C.; Manzke, R. Charge-Density-Wave Phase of $1T-TiSe_2$: The Influence of Conduction Band Population. *Phys. Rev. Lett.* **2011**, *107*, 176405. [CrossRef]
68. Titov, A.N.; Kuznetsov, M.V.; Razinkin, A.S. On the nature of state with a charge-density wave in $TiSe_2$ from data of scanning tunneling microscopy. *Phys. Solid State* **2011**, *53*, 1073–1077. [CrossRef]
69. Knowles, P.; Yang, B.; Muramatsu, T.; Moulding, O.; Buhot, J.; Sayers, C.J.; Da Como, E.; Friedemann, S. Fermi surface reconstruction and electron dynamics at the charge-density-wave transition in $TiSe_2$. *Phys. Rev. Lett.* **2020**, *124*, 167602. [CrossRef]
70. Bussmann-Holder, A.; Büttner, H. Charge-density-wave formation in $TiSe_2$ driven by an incipient antiferroelectric instability. *J. Phys. Condens. Matter* **2002**, *14*, 7973. [CrossRef]
71. Rohde, G.; Rohwer, T.; Stange, A.; Sohrt, C.; Hanff, K.; Yang, L.X.; Kipp, L.; Rossnagel, K.; Bauer, M. Does the excitation wavelength affect the ultrafast quenching dynamics of the charge-density wave in $1T$-$TiSe_2$? *J. Electron Spectrosc. Relat. Phenom.* **2014**, *195*, 244–248. [CrossRef]
72. Mulazzi, M.; Chainani, A.; Katayama, N.; Eguchi, R.; Matsunami, M.; Ohashi, H.; Senba, Y.; Nohara, M.; Uchida, M.; Takagi, H.; et al. Absence of nesting in the charge-density-wave system $1T$-VS_2 as seen by photoelectron spectroscopy. *Phys. Rev. B* **2010**, *82*, 075130. [CrossRef]
73. Gauzzi, A.; Sellam, A.; Rousse, G.; Klein, Y.; Taverna, D.; Giura, P.; Calandra, M.; Loupias, G.; Gozzo, F.; Gilioli, E.; et al. Possible phase separation and weak localization in the absence of a charge-density wave in single-phase $1T$-VS_2. *Phys. Rev. B* **2014**, *89*, 235125. [CrossRef]
74. Kim, H.J.; Choi, B.K.; Lee, I.H.; Kim, M.J.; Chun, S.H.; Jozwiak, C.; Bostwick, A.; Rotenberg, E.; Chang, Y.J. Electronic structure and charge-density wave transition in monolayer VS_2. *Curr. Appl. Phys.* **2021**, *30*, 8–13. [CrossRef]
75. Van Efferen, C.; Berges, J.; Hall, J.; van Loon, E.; Kraus, S.; Schobert, A.; Wekking, T.; Huttmann, F.; Plaar, E.; Rothenbach, N.; et al. A full gap above the Fermi level: The charge density wave of monolayer VS_2. *arXiv* **2021**, arXiv:2101.01140. [CrossRef] [PubMed]
76. Isaacs, E.B.; Marianetti, C.A. Electronic correlations in monolayer VS_2. *Phys. Rev. B* **2016**, *94*, 035120. [CrossRef]
77. Yang, J.; Wang, W.; Liu, Y.; Du, H.; Ning, W.; Zheng, G.; Jin, C.; Han, Y.; Wang, N.; Yang, Z. Thickness dependence of the charge-density-wave transition temperature in VSe_2. *Appl. Phys. Lett.* **2014**, *105*, 063109. [CrossRef]
78. Feng, J.; Biswas, D.; Rajan, A.; Watson, M.D.; Mazzola, F.; Clark, O.J.; Underwood, K.; Markovic, I.; McLaren, M.; Hunter, A. Electronic Structure and Enhanced Charge-Density Wave Order of Monolayer VSe_2. *Nano Lett.* **2018**, *18*, 4493–4499. [CrossRef]
79. Coelho, P.M.; Nguyen Cong, K.; Bonilla, M.; Kolekar, S.; Phan, M.H.; Avila, J.; Asensio, M.C.; Oleynik, I.I.; Batzill, M. Charge density wave state suppresses ferromagnetic ordering in VSe_2 monolayers. *J. Phys. Chem. C* **2019**, *123*, 14089–14096. [CrossRef]
80. Fumega, A.O.; Gobbi, M.; Dreher, P.; Wan, W.; Gonzalez-Orellana, C.; Peña-Diaz, M.; Rogero, C.; Herrero-Martín, J.; Gargiani, P.; Ilyn, M.; et al. Absence of ferromagnetism in VSe_2 caused by its charge density wave phase. *J. Phys. Chem. C* **2019**, *123*, 27802–27810. [CrossRef]
81. Duvjir, G.; Choi, B.K.; Ly, T.T.; Lam, N.H.; Jang, K.; Dang, D.D.; Chang, Y.J.; Kim, J. Multiple charge density wave phases of monolayer VSe_2 manifested by graphene substrates. *Nanotechnology* **2021**, *32*, 364002. [CrossRef]
82. Yan, J.-A.; Cruz, M.A.D.; Cook, B.; Varga, K. Structural, electronic and vibrational properties of few-layer $2H$-and $1T$-$TaSe_2$. *Sci. Rep.* **2015**, *5*, 16646. [CrossRef] [PubMed]
83. Hohenberg, P.; Kohn, W. Inhomogeneous electron gas. *Phys. Rev.* **1964**, *136*, B864. [CrossRef]
84. Kohn, W.; Sham, L.J. Self-consistent equations including exchange and correlation effects. *Phys. Rev.* **1965**, *140*, A1133. [CrossRef]
85. Motizuki, K.; Suzuki, N.; Yoshida, Y.; Takaoka, Y. Role of electron-lattice interaction in lattice dynamics and lattice instability of $1T$-$TiSe_2$. *Solid State Commun.* **1981**, *40*, 995–998. [CrossRef]
86. Giannozzi, P.; Baroni, S.; Bonini, N.; Calandra, M.; Car, R.; Cavazzoni, C.; Ceresoli, D.; Chiarotti, G.L.; Cococcioni, M.; Dabo, I.; et al. QUANTUM ESPRESSO: A modular and open-source software project for quantum simulations of materials. *J. Phys. Condens. Matter* **2009**, *21*, 395502. [CrossRef]
87. Giannozzi, O.P.; Andreussi, T.; Brumme, O.; Bunau, M.; Buongiorno Nardelli, M.; Calandra, R.; Car, C.; Cavazzoni, D.; Ceresoli, M.; Cococcioni, N.; et al. Advanced capabilities for materials modelling with Quantum ESPRESSO. *J. Phys. Condens. Matter* **2017**, *29*, 465901. [CrossRef]
88. Giannozzi, O.P.; Baseggio, P.; Bonfà, D.; Brunato, R.; Car, I.; Carnimeo, C.; Cavazzoni, S.; de Gironcoli, P.; Delugas, F.; Ferrari Ruffino, A.; et al. QUANTUM ESPRESSO: A modular and open-source software project for quantum simulations of materials. *J. Chem. Phys.* **2020**, *152*, 154105. [CrossRef]

89. Perdew, J.P.; Wang, Y. Accurate and simple analytic representation of the electron-gas correlation energy. *Phys. Rev. B* **1992**, *45*, 13244. [CrossRef]
90. Fuchs, M.; Scheffler, M. Ab initio pseudopotentials for electronic structure calculations of poly-atomic systems using density-functional theory. *Comput. Phys. Commun.* **1999**, *119*, 67–98. [CrossRef]
91. Troullier, N.; Martins, J.L. Efficient pseudopotentials for plane-wave calculations. *Phys. Rev. B* **1991**, *43*, 1993. [CrossRef]
92. Rydberg, H.; Dion, M.; Jacobson, N.; Schröder, E.; Hyldgaard, P.; Simak, S.; Langreth, D.C.; Lundqvist, B.I. Van der Waals density functional for layered structures. *Phys. Rev. Lett.* **2003**, *91*, 126402. [CrossRef]
93. Thonhauser, T.; Cooper, V.R.; Li, S.; Puzder, A.; Hyldgaard, P.; Langreth, D.C. Van der Waals density functional: Self-consistent potential and the nature of the van der Waals bond. *Phys. Rev. B* **2007**, *76*, 125112. [CrossRef]
94. Berland, K.; Cooper, V.R.; Lee, K.; Schröder, E.; Thonhauser, T.; Hyldgaard, P.; Lundqvist, B.I. van der Waals forces in density functional theory: A review of the vdW-DF method. *Rep. Prog. Phys.* **2015**, *78*, 066501. [CrossRef]
95. Berland, K.; Arter, C.A.; Cooper, V.R.; Lee, K.; Lundqvist, B.I.; Schröder, E.; Thonhauser, T.; Hyldgaard, P. van der Waals density functionals built upon the electron-gas tradition: Facing the challenge of competing interactions. *J. Chem. Phys.* **2014**, *140*, 18A539. [CrossRef] [PubMed]
96. Garrity, K.F.; Chowdhury, S.; Tavazza, F.M. Topological surface states of MnBi2Te4 at finite temperatures and at domain walls. *Phys. Rev. Mater.* **2021**, *5*, 024207. [CrossRef]
97. Feldman, J.L.; Vold, C.L.; Skelton, E.F.; Yu, S.C.; Spain, I.L. X-ray diffraction studies and thermal and elastic properties of 2*H*-$TaSe_2$. *Phys. Rev. B* **1978**, *18*, 5820. [CrossRef]
98. Givens, F.L.; Fredericks, G.E. Thermal expansion op $NbSe_2$ and TaS_2. *J. Phys. Chem. Solids* **1977**, *38*, 1363–1365. [CrossRef]
99. Janner, T.; Janssen, P.; de Wolff, M. Incommensurate Crystals: A New Phase in Solid State Physics. *Europhys. News* **1982**, *13*, 1. [CrossRef]
100. Perdew, J.P.; Zunger, A. Self-interaction correction to density-functional approximations for many-electron systems. *Phys. Rev. B* **1981**, *23*, 5048. [CrossRef]
101. Rappe, A.M.; Rabe, K.M.; Kaxiras, E.; Joannopoulos, J. Optimized pseudopotentials. *Phys. Rev. B* **1990**, *41*, 1227. [CrossRef]
102. Grinberg, I.; Ramer, N.J.; Rappe, A.M. Transferable relativistic Dirac-slater pseudopotentials. *Phys. Rev. B* **2000**, *62*, 2311. [CrossRef]
103. Vanderbilt, D. Soft self-consistent pseudopotentials in a generalized eigenvalue formalism. *Phys. Rev. B* **1990**, *41*, 7892. [CrossRef]
104. Kresse, G.; Joubert, D. From ultrasoft pseudopotentials to the projector augmented-wave method. *Phys. Rev. B* **1999**, *59*, 1758. [CrossRef]
105. Mermin, N.D. Thermal properties of the inhomogeneous electron gas. *Phys. Rev.* **1965**, *137*, A1441. [CrossRef]
106. Kohn, W. Image of the Fermi Surface in the Vibration Spectrum of a Metal. *Phys. Rev. Lett.* **1959**, *2*, 393. [CrossRef]
107. Duong, D.L.; Burghard, M.; Schön, J.C. Ab initio computation of the transition temperature of the charge density wave transition in $TiSe_2$. *Phys. Rev. B* **2015**, *92*, 245131. [CrossRef]
108. Hill, H.M.; Chowdhury, S.; Simpson, J.R.; Rigosi, A.F.; Newell, D.B.; Berger, H.; Tavazza, F.; Walker, A.F.R.H. Phonon origin and lattice evolution in charge density wave states. *Phys. Rev. B* **2019**, *99*, 174110. [CrossRef] [PubMed]
109. Joshi, J.; Hill, H.M.; Chowdhury, S.; Malliakas, C.D.; Tavazza, F.; Chatterjee, U.; Walker, A.F.R.H.; Vora, P.M. Short-range charge density wave order in 2*H*−TaS_2. *Phys. Rev. B* **2019**, *99*, 245144. [CrossRef]
110. Hajiyev, P.; Cong, C.; Qiu, C.; Yu, T. Contrast and Raman spectroscopy study of single-and few-layered charge density wave material: 2*H*-$TaSe_2$. *Sci. Rep.* **2013**, *3*, 1–6. [CrossRef] [PubMed]
111. Reshak, A.H.; Auluck, S. Full-potential calculations of the electronic and optical properties for 1*T* and 2*H* phases of TaS_2 and $TaSe_2$. *Phys. B Condens. Matter* **2005**, *358*, 158–165. [CrossRef]
112. Blaha, P.; Schwartz, K.; Sorantin, P.; Trickey, S.B. Full-potential, linearized augmented plane wave programs for crystalline systems. *Comput. Phys. Commun.* **1990**, *59*, 399. [CrossRef]
113. Guo, G.Y.; Liang, W.Y. Electronic structures of intercalation complexes of the layered compound 2*H*-TaS_2. *J. Phys. C Solid State Phys.* **1987**, *20*, 4315. [CrossRef]
114. Lazar, P.; Martincová, J.; Otyepka, M. Structure, dynamical stability, and electronic properties of phases in TaS_2 from a high-level quantum mechanical calculation. *Phys. Rev. B* **2015**, *92*, 224104. [CrossRef]
115. Martincová, J.; Otyepka, M.; Lazar, P. Atomic-Scale Edge Morphology, Stability, and Oxidation of Single-Layer 2*H*-TaS_2. *ChemPlusChem* **2020**, *85*, 2557–2564. [CrossRef]
116. Hinsche, N.F.; Thygesen, K.S. Electron–phonon interaction and transport properties of metallic bulk and monolayer transition metal dichalcogenide TaS_2. *2D Mater.* **2017**, *5*, 015009. [CrossRef]
117. Dion, M.; Rydberg, H.; Schröder, E.; Langreth, D.C.; Lundqvist, B.I. Van der Waals density functional for general geometries. *Phys. Rev. Lett.* **2004**, *92*, 246401. [CrossRef]
118. Sanders, C.E.; Dendzik, M.; Ngankeu, A.S.; Eich, A.; Bruix, A.; Bianchi, M.; Miwa, J.A.; Hammer, B.; Khajetoorians, A.A.; Hofmann, P. Crystalline and electronic structure of single-layer TaS_2. *Phys. Rev. B* **2016**, *94*, 081404. [CrossRef]
119. Cain, J.D.; Oh, S.; Azizi, A.; Stonemeyer, S.; Dogan, M.; Thiel, M.; Ercius, P.; Cohen, M.L.; Zettl, A. Ultranarrow TaS_2 Nanoribbons. *Nano Lett.* **2021**, *21*, 3211–3217. [CrossRef]
120. Smith, N.V.; Kevan, S.D.; DiSalvo, F.J. Band structures of the layer compounds 1*T*-TaS_2 and 2*H*-$TaSe_2$ in the presence of commensurate charge-density waves. *J. Phys. C Solid State Phys.* **1985**, *18*, 3175. [CrossRef]

121. Campagnoli, G.; Gustinetti, A.; Stella, A.; Tosatti, E. Optical response, band structure, plasmons, and charge density waves in 2*H*-$TaSe_2$. *Phys. B Condens. Matter* **1980**, *99*, 271–275. [CrossRef]
122. Woolley, A.M.; Wexler, G. Band structures and Fermi surfaces for 1*T*-TaS_2, 1*T*-$TaSe_2$ and 1*T*-VSe_2. *J. Phys. C Solid State Phys.* **1977**, *10*, 2601. [CrossRef]
123. Giambattista, B.; Slough, C.G.; McNairy, W.W.; Coleman, R.V. Scanning tunneling microscopy of atoms and charge-density waves in 1*T*-TaS_2, 1*T*-$TaSe_2$, and 1*T*-VSe_2. *Phys. Rev. B* **1990**, *41*, 10082. [CrossRef] [PubMed]
124. Motizuki, K.; Ando, E. Theoretical Study of Lattice Instability and Lattice Dynamics of 2*H*-$TaSe_2$ and 2*H*-$NbSe_2$. I. Electron-Lattice Interaction and Generalized Electronic Susceptibility. *J. Phys. Soc. Jpn.* **1983**, *52*, 2849–2857. [CrossRef]
125. Myron, H.W.; Freeman, A.J. Electronic structure and Fermi-surface-related instabilities in 1*T*−TaS_2 and 1*T*−$TaSe_2$. *Phys. Rev. B* **1975**, *11*, 2735. [CrossRef]
126. Wertheim, G.K.; DiSalvo, F.J.; Chiang, S. Sign and amplitude of charge density waves in 1*T*−TaS_2 and $TaSe_2$. *Phys. Lett. A* **1975**, *54*, 304–306. [CrossRef]
127. Samnakay, R.; Wickramaratne, D.; Pope, T.R.; Lake, R.K.; Salguero, T.T.; Balandin, A.A. Zone-folded phonons and the commensurate–incommensurate charge-density-wave transition in 1*T*-$TaSe_2$ thin films. *Nano Lett.* **2015**, *15*, 2965–2973. [CrossRef]
128. Ge, Y.; Liu, A.Y. First-principles investigation of the charge-density-wave instability in 1*T*-$TaSe_2$. *Phys. Rev. B* **2010**, *82*, 155133. [CrossRef]
129. Albertini, O.R.; Liu, A.Y.; Calandra, M. Effect of electron doping on lattice instabilities in single-layer 1*H*-TaS_2. *Phys. Rev. B* **2017**, *95*, 235121. [CrossRef]
130. Ryu, H.; Chen, Y.; Kim, H.; Tsai, H.Z.; Tang, S.; Jiang, J.; Liou, F.; Kahn, S.; Jia, C.; Omrani, A.A.; et al. Persistent charge-density-wave order in single-layer $TaSe_2$. *Nano Lett.* **2018**, *18*, 689–694. [CrossRef]
131. Hill, H.M.; Rigosi, A.F.; Chowdhury, S.; Yang, Y.; Nguyen, N.V.; Tavazza, F.; Elmquist, R.E.; Newell, D.B.; Walker, A.F.R.H. Probing the dielectric response of the interfacial buffer layer in epitaxial graphene via optical spectroscopy. *Phys. Rev. B* **2017**, *96*, 195437. [CrossRef]
132. Park, J.W.; Yeom, H.W. Atomic structures and electronic correlation of monolayer 1*T*-$TaSe_2$. *arXiv* **2020**, arXiv:2008.05702.
133. Albertini, O.R.; Zhao, R.; McCann, R.L.; Feng, S.; Terrones, M.; Freericks, J.K.; Robinson, J.A.; Liu, A.Y. Zone-center phonons of bulk, few-layer, and monolayer 1*T*−TaS_2: Detection of commensurate charge density wave phase through Raman scattering. *Phys. Rev. B* **2016**, *93*, 2141. [CrossRef]
134. Hall, J.; Ehlen, N.; Berges, J.; van Loon, E.; van Efferen, C.; Murray, C.; Rosner, M.; Li, J.; Senkovskiy, B.V.; Hell, M.; et al. Environmental control of charge density wave order in monolayer 2*H*-TaS_2. *ACS Nano* **2019**, *13*, 10210–10220. [CrossRef]
135. Lefcochilos-Fogelquist, H.M.; Albertini, O.R.; Liu, A.Y. Substrate-Induced Suppression of Charge Density Wave Phase in Monolayer 1*H*-TaS_2 on Au(111). *Phys. Rev. B* **2019**, *99*, 174113. [CrossRef]
136. Mijin, S.D.; Baum, A.; Bekaert, J.; Šolajić, A.; Pešić, J.; Liu, Y.; He, G.; Milošević, M.V.; Petrovic, C.; Popović, Z.V.; et al. Probing charge density wave phases and the Mott transition in 1*T*-TaS_2 by inelastic light scattering. *Phys. Rev. B* **2021**, *103*, 245133. [CrossRef]
137. Perdew, J.P.; Chevary, J.A.; Vosko, S.H.; Jackson, K.A.; Pederson, M.R.; Singh, D.J.; Fiolhais, C. Atoms, molecules, solids, and surfaces: Applications of the generalized gradient approximation for exchange and correlation. *Phys. Rev. B* **1992**, *46*, 6671. [CrossRef]
138. Chakraborty, B.; Matte, H.R.; Sood, A.K.; Rao, C.N.R. Layer-dependent resonant Raman scattering of a few layer MoS_2. *J. Raman Spectrosc.* **2013**, *44*, 92–96. [CrossRef]
139. Livneh, T.; Spanier, J.E. A comprehensive multiphonon spectral analysis in MoS_2. *2D Mater.* **2015**, *2*, 035003. [CrossRef]
140. Carvalho, B.R.; Wang, Y.; Mignuzzi, S.; Roy, D.; Terrones, M.; Fantini, C.; Crespi, V.H.; Malard, L.M.; Pimenta, M.A. Intervalley scattering by acoustic phonons in two-dimensional MoS_2 revealed by double-resonance Raman spectroscopy. *Nat. Commun.* **2017**, *8*, 1–8. [CrossRef] [PubMed]
141. Sekine, T.; Uchinokura, K.; Nakashizu, T.; Matsuura, E.; Yoshizaki, R. Dispersive Raman mode of layered compound 2*H*-MoS_2 under the resonant condition. *J. Phys. Soc. Jpn.* **1984**, *53*, 811–818. [CrossRef]
142. Klein, M.V. Theory of two-phonon Raman scattering in transition metals and compounds. *Phys. Rev. B* **1981**, *24*, 4208. [CrossRef]
143. Kawabata, A. Green Function Theory of Raman Scattering. *J. Phys. Soc. Jpn.* **1971**, *30*, 68–85. [CrossRef]
144. Venezuela, P.; Lazzeri, M.; Mauri, F. Theory of double-resonant Raman spectra in graphene: Intensity and line shape of defect-induced and two-phonon bands. *Phys. Rev. B* **2011**, *84*, 035433. [CrossRef]
145. Motizuki, K.; Kimura, K.; Suzuki, N. Theoretical Study of Lattice Instability and Lattice Dynamics of 2*H*-$TaSe_2$ and 2*H*-$NbSe_2$ II. Lattice Dynamics and Phonon Anomalies. *J. Phys. Soc. Jpn.* **1984**, *53*, 1078–1086. [CrossRef]
146. Nakashizu, T.; Sekine, T.; Uchinokura, K.; Matsuura, E. Raman study of charge-density-wave phase transitions in 4Hb-$TaSe_2$. *J. Phys. Soc. Jpn.* **1986**, *55*, 672–682. [CrossRef]
147. Lee, P.A.; Rice, T.M.; Anderson, P.W. Conductivity from charge or spin density waves. *Solid State Commun.* **1993**, *88*, 1001–1007. [CrossRef]
148. Chowdhury, S.; Simpson, J.R.; Einstein, T.L.; Walker, A.F.R.H. Strain-controlled magnetic and optical properties of monolayer 2*H*−$TaSe_2$. *Phys. Rev. Mater.* **2019**, *3*, 084004. [CrossRef]
149. Wang, H.; Chen, Y.; Zhu, C.; Wang, X.; Zhang, H.; Tsang, S.H.; Li, H.; Lin, J.; Yu, T.; Liu, Z.; et al. Synthesis of Atomically Thin 1*T*-$TaSe_2$ with a Strongly Enhanced Charge-Density-Wave Order. *Adv. Funct. Mater.* **2020**, *30*, 2001903. [CrossRef]

150. Dobal, P.S.; Dixit, A.; Katiyar, R.S.; Yu, Z.; Guo, R.; Bhalla, A.S. Micro-Raman scattering and dielectric investigations of phase transition behavior in the $BaTiO_3$-$BaZrO_3$ system. *J. Appl. Phys.* **2001**, *89*, 8085. [CrossRef]
151. Yoshida, M.; Zhang, Y.; Ye, J.; Suzuki, R.; Imai, Y.; Kimura, S.; Fujiwara, A.; Iwasa, Y. Controlling charge-density-wave states in nano-thick crystals of 1*T*-TaS_2. *Sci. Rep.* **2014**, *4*, 7302. [CrossRef]
152. Yamada, K.; Souma, S.; Yamauchi, K.; Shimamura, N.; Sugawara, K.; Trang, C.X.; Oguchi, T.; Ueno, K.; Takahashi, T.; Sato, T. Ultrathin Bismuth Film on 1*T*-TaS_2: Structural Transition and Charge-Density-Wave Proximity Effect. *Nano Lett.* **2018**, *18*, 3235–3240. [CrossRef] [PubMed]
153. Yang, Y.; Fang, S.; Fatemi, V.; Ruhman, J.; Navarro-Moratalla, E.; Watanabe, K.; Taniguchi, T.; Kaxiras, E.; Jarillo-Herrero, P. Enhanced superconductivity upon weakening of charge density wave transport in 2*H*-TaS_2 in the two-dimensional limit. *Phys. Rev. B* **2018**, *98*, 035203. [CrossRef]
154. Neto, A.C. Charge density wave, superconductivity, and anomalous metallic behavior in 2D transition metal dichalcogenides. *Phys. Rev. Lett.* **2001**, *86*, 4382. [CrossRef] [PubMed]
155. Koley, S.; Mohanta, N.; Taraphder, A. Charge density wave and superconductivity in transition metal dichalcogenides. *Eur. Phys. J. B* **2020**, *93*, 1–8. [CrossRef]
156. Ishiguro, Y.; Bogdanov, K.; Kodama, N.; Ogiba, M.; Ohno, T.; Baranov, A.; Takai, K. Layer Number Dependence of Charge Density Wave Phase Transition Between Nearly-Commensurate and Incommensurate Phases in 1*T*-TaS_2. *J. Phys. Chem. C* **2020**, *124*, 27176–27184. [CrossRef]
157. Kühn, D.; Müller, M.; Sorgenfrei, F.; Giangrisostomi, E.; Jay, R.M.; Ovsyannikov, R.; Mårtensson, N.; Sánchez-Portal, D.; Föhlisch, A. Directional sub-femtosecond charge transfer dynamics and the dimensionality of 1*T*-TaS_2. *Sci. Rep.* **2019**, *9*, 1–9. [CrossRef] [PubMed]
158. Soler, J.M.; Artacho, E.; Gale, J.D.; García, A.; Junquera, J.; Ordejón, P.; Sánchez-Portal, D. The SIESTA method for ab initio order-N materials simulation. *J. Phys. Condens. Matter* **2002**, *14*, 2745. [CrossRef]
159. Klimeš, J.; Bowler, D.R.; Michaelides, A. Chemical accuracy for the van der Waals density functional. *J. Phys. Condens. Matter* **2009**, *22*, 022201. [CrossRef]
160. Sato, H.; Arita, M.; Utsumi, Y.; Mukaegawa, Y.; Sasaki, M.; Ohnishi, A.; Kitaura, M.; Namatame, H.; Taniguchi, M. Conduction-band electronic structure of 1*T*-TaS_2 revealed by angle-resolved inverse-photoemission spectroscopy. *Phys. Rev. B* **2014**, *89*, 155137. [CrossRef]
161. Claessen, R.; Burandt, B.; Carstensen, H.; Skibowski, M. Conduction-band structure and charge-density waves in 1*T*-TaS_2. *Phys. Rev. B* **1990**, *41*, 8270. [CrossRef]
162. Chowdhury, S.; Hill, H.M.; Rigosi, A.F.; Briggs, A.; Berger, H.; Newell, D.B.; Hight Walker, A.F.R.; Tavazza, F. Examining Experimental Raman Mode Behavior in Mono-and Bilayer 2*H*-$TaSe_2$ via Density Functional Theory: Implications for Quantum Information Science. *ACS Appl. Nano Mater.* **2021**, *4*, 1810–1816. [CrossRef] [PubMed]
163. Chowdhury, S.; Rigosi, A.F.; Hill, H.M.; Briggs, A.; Newell, D.B.; Berger, H.; Hight Walker, A.F.R.; Tavazza, F. Influence of Dimensionality on the Charge Density Wave Phase of 2*H*-$TaSe_2$. *arXiv* **2020**, arXiv:2005.11350.
164. Yoshida, M.; Suzuki, R.; Zhang, Y.; Nakano, M.; Iwasa, Y. Memristive phase switching in two-dimensional 1*T*-TaS_2 crystals. *Sci. Adv.* **2015**, *1*, e1500606. [CrossRef]
165. Chen, P.; Chan, Y.H.; Fang, X.Y.; Zhang, Y.; Chou, M.Y.; Mo, S.K.; Hussain, Z.; Fedorov, A.V.; Chiang, T.C. Charge density wave transition in single-layer titanium diselenide. *Nat. Commun.* **2015**, *6*, 1–5. [CrossRef] [PubMed]
166. Ji, S.; Gråsäs, O.; Rossnagel, K.; Weissenrieder, J. Transient three-dimensional structural dynamics in 1*T*-$TaSe_2$. *Phys. Rev. B* **2020**, *101*, 094303. [CrossRef]
167. Dewhurst, K.; Sharma, S.; Nordström, L.; Cricchio, F.; Bultmark, F.; Granas, O.; Gross, H. Elk FP-LAPW Code. 2018. Available online: http://elk.sourceforge.net/ (accessed on 14 December 2021).
168. Lin, D.; Li, S.; Wen, J.; Berger, H.; Forró, L.; Zhou, H.; Jia, S.; Taniguchi, T.; Watanabe, K.; Xi, X.; et al. Patterns and driving forces of dimensionality-dependent charge density waves in 2*H*-type transition metal dichalcogenides. *Nat. Commun.* **2020**, *11*, 1–9. [CrossRef]